

# Material mixing in pulsar wind nebulae of massive runaway stars

D. M.-A. Meyer<sup>★1</sup> and D. F. Torres<sup>†1,2,3</sup>

<sup>1</sup> *Institute of Space Sciences (ICE, CSIC), Campus UAB, Carrer de Can Magrans s/n, 08193 Barcelona, Spain*

<sup>2</sup> *Institut d'Estudis Espacials de Catalunya (IEEC), 08860 Barcelona, Spain*

<sup>3</sup> *Institució Catalana de Recerca i Estudis Avançats (ICREA), Barcelona, Spain*

Last updated 2020 June 10; in original form 2013 September 5

## ABSTRACT

In this study we quantitatively examine the manner pulsar wind, supernova ejecta and defunct stellar wind materials distribute and melt together into plerions. We performed 2.5D MHD simulations of the entire evolution of their stellar surroundings and different scenarios are explored, whether the star dies as a red supergiant and Wolf-Rayet supernova progenitors, and whether it moved with velocity  $20 \text{ km s}^{-1}$  or  $40 \text{ km s}^{-1}$  through the ISM. Within the post-explosion, early 10 kyr, the H-burning-products rich red supergiant wind only mixes by  $\leq 20\%$ , due to its dense circumstellar medium filling the progenitor's bow shock trail, still unaffected by the supernova blastwave. Wolf-Rayet materials, enhanced in C, N, O elements, distribute circularly for the  $35 M_{\odot}$  star moving at  $20 \text{ km s}^{-1}$  and oblongly at higher velocities, mixing efficiently up to 80%. Supernova ejecta, filled with Mg, Si, Ca, Ti and Fe, remain spherical for longer times at  $20 \text{ km s}^{-1}$  but form complex patterns at higher progenitor speeds due to earlier interaction with the bow shock, in which they mix more efficiently. The pulsar wind mixing is more efficient for Wolf-Rayet (25%) than red supergiant progenitors (20%). This work reveals that the past evolution of massive stars and their circumstellar environments critically shapes the internal distribution of chemical elements on plerionic supernova remnants, and, therefore, governs the origin of the various emission mechanisms at work therein. This is essential for interpreting multi-frequency observations of atomic and molecular spectral lines, such as in optical, infrared, and soft X-rays.

**Key words:** methods: MHD – stars: evolution – stars: massive – ISM: supernova remnants.

## 1 INTRODUCTION

Massive stars form in dense, opaque molecular clouds which contracts under their own gravity. Once local gravitational collapse takes place and form a stellar embryo, the conservation of momentum organises the infalling material as an accretion disc, which fragments. Its debris feed the growing protostar, inducing luminous flares and forming companions (Meyer et al. 2019; Meyer & Vorobyov 2024). When the gravity of the massive protostar is sufficiently important, fusion nuclear reactions ignite in its core, expelling strong stellar winds and radiation from its surface, which dissipate the molecular environment and shape it as wind bubbles (Weaver et al. 1977). If the star moves fast enough, the bubble is distorted as an arc-like nebula called bow shock (Gull & Sofia 1979; Wilkin 1996). The circumstellar medium of massive stars continues reflecting stellar feedback throughout their entire evolution, e.g. as a red supergiant or a Wolf-Rayet object, see Avedisova (1972); Smith et al. (1984); Noriega-Crespo et al. (1997). Some high-mass stars, at the end of their lives, explode as a core-collapse supernova, releasing energy and mass into their pre-shaped surroundings. The meeting of the supernova blastwave with the wind nebula produces a supernova remnant, and additionally, when a compact object such as a rotating magnetized neutron star form as the ultimate rest of the massive

star, a relativistic wind power the so-called plerionic supernova remnant (Weiler & Shaver 1978; Caswell 1979; Weiler & Panagia 1980; Gaensler & Slane 2006; Kargaltsev et al. 2017a).

In addition to a growing accumulation of multi-wavelengths observations, see e.g. (Hester 2008; Bühler & Blandford 2014; Bock et al. 1998; Kargaltsev & Pavlov 2007; Kargaltsev et al. 2012, 2017b; Frail & Scharringhausen 1997; ?; Popov et al. 2019; ?; ?; Turner et al. 2024), the understandings of pulsar wind nebulae and pulsar-powered supernova remnants is inseparable from the development of numerical simulations. Series of 1-dimensional works (Kennel & Coroniti 1984; Coroniti 1990; Begelman & Li 1992; Begelman 1998), 2-dimensional models Komissarov & Lyubarsky (2003, 2004); van der Swaluw et al. (2003, 2004); Komissarov (2006); Del Zanna et al. (2006); Camus et al. (2009); Komissarov & Lyutikov (2011); Olmi et al. (2014), 3-dimensional studies (Porth et al. 2013, 2014; Olmi et al. 2016) and applications to the plerions Geminga and Vela have been performed (Hester 2008; Bühler & Blandford 2014; Bock et al. 1998; Popov et al. 2019; ?), deepening our comprehension of the internal functioning of pulsar wind nebulae, from the magnetosphere to the pc-scale environment. The reverberation phase of the pulsar wind termination shock Bandiera et al. (2020, 2023, ?), and the motion of the pulsar inside of the supernova remnant (Temim et al. 2015, 2017; Kolb et al. 2017; Temim et al. 2022) and beyond, into the ISM (Bucciantini & Bandiera 2001; Bucciantini 2018; Toropina et al. 2019), have been particularly focused upon.

Until now, numerical simulations of pulsar wind nebulae have

★ E-mail: meyer@ice.csic.es

† E-mail: dtorres@ice.csic.es

not considered the detailed chemical composition of the various materials involved in the problem, which correspond to the wind blown during the main-sequence, red supergiant, and Wolf-Rayet evolutionary phases of the progenitor, as well as to the supernova ejecta released after the explosion (Maeder & Meynet 2000). Mixing of the dominant chemical species of each component will happen at the unstable discontinuities separating the various regions. Massive stars spend most of their lives in a long main-sequence phase, during which both the surface chemical composition and the composition of the accelerated stellar wind are primarily made up of hydrogen (H). As main-sequence massive stars evolve into the red supergiant phase, the composition of the stellar surface continues to be dominated by H-atoms, even though their cores are depleted of H and begin to fuse helium (He). Towards the end of the supergiant phase, the surface becomes enriched in He to a level comparable to that of H. The winds of red supergiants are enriched in nitrogen (N) and sulfur (S), as evidenced by the emission lines observed from the bow shock nebula of the runaway red supergiant IRC-10414 (Cox et al. 2012; Meyer et al. 2014; Gvaramadze et al. 2014; Meyer et al. 2021).

If the stellar mass is sufficiently high, its radius, surface, and wind properties evolve again as the star enters the Wolf-Rayet evolutionary phase (Maeder & Meynet 2000). Throughout this phase, carbon (C), neon (Ne), magnesium (Mg), followed by oxygen (O) and finally silicon (Si), are produced by nuclear fusion, generating an iron (Fe) core that ignites the final mechanism for a core-collapse supernova explosion (Smartt 2009; Janka et al. 2016). The winds of Wolf-Rayet stars are enriched in He, C, N and O (Hamann et al. 2006) and, in their turn, enrich their circumstellar medium accordingly (Maeder 2009; Berlanas et al. 2018; Schulreich et al. 2023; Gómez-González et al. 2022). The respective proportions of the chemical yields constituting the winds of massive stars are further affected by their zero-age main-sequence stellar rotation and the metallicity of their native environment (Mokiem et al. 2007; Brott et al. 2011; Vink & Sander 2021; Marcolino et al. 2024). Notably, the most massive stars with initial masses  $\geq 100 M_{\odot}$  can process heavy nuclei in their cores via the sodium-neon (Na-Ne) and magnesium-aluminum (Mg-Al) cycles, releasing this aluminum (Al) excess into their winds and replenishing the interstellar medium with it (Dearborn & Blake 1984).

The supernova explosion releases all these chemical elements into the circumstellar medium (McKee & Cowie 1975; Martizzi et al. 2015; Orlando et al. 2019, 2021, 2020, 2022a,b) when the blast wave collides with the wind nebula formed throughout the star's life, resulting in a supernova remnant that is eventually powered by a pulsar wind (Weiler & Shaver 1978; Caswell 1979; Weiler & Panagia 1980; Reynolds & Chevalier 1984; Slane 2017). The distribution of chemical species within plerions is therefore governed by the local conditions of the interstellar medium, the stellar evolution history of the progenitor, the properties of the explosion and the characteristics of the pulsar. These interstellar, circumstellar and ejecta chemical elements, ruling the local cooling and heating processes of the gas by atomic and molecular emission (Wolfire et al. 2003; Teşileanu et al. 2008; Wiersma et al. 2009), which generate X-rays, radio, infrared and optical emission, mostly produced by H, He, O, Fe and a plethora of other atoms, ions and molecules (Whiteoak & Green 1996; Reach et al. 2006; Seok et al. 2013). An example of such supernova remnant is the Cygnus Loop and its ejecta distribution of heavy elements (Uchida et al. 2009).

The chemical stellar wind history is therefore a factor that can not be excluded when modelling the long-term ( $> 10$  kyr) evolution of pulsar wind nebulae to understand their emission. Numerical simulations provided so far two examples. First, that of a runaway

**Table 1.** List of numerical models. All simulations assume a rotating massive progenitor of zero-age main-sequence mass  $M_{\star}$  (in  $M_{\odot}$ ) at solar metallicity and moving with velocity  $v_{\star}$  through the warm phase of the Galactic plane. The table indicate the stellar evolution history in each model, from the MS (main-sequence) phase to the final SN (supernova) explosion and ultimate PWN (pulsar wind), through the RSG (red supergiant) and Wolf-Rayet stages.

Model	Evolution history
PWN – 20 $M_{\odot}$ – v20 – mix	MS → RSG → SN → PWN
PWN – 20 $M_{\odot}$ – v40 – mix	MS → RSG → SN → PWN
PWN – 35 $M_{\odot}$ – v20 – mix	MS → RSG → WR → SN → PWN
PWN – 35 $M_{\odot}$ – v40 – mix	MS → RSG → WR → SN → PWN

supernova progenitor which wind-ISM produces a stellar wind bow shock inducing asymmetries in the pulsar wind nebula (Meyer & Meliani 2022). Secondly, the case of a static massive star having the termination shock of its stellar wind bubble elongated by the organised magnetic field of the ISM. The resulting pulsar wind nebula develops in its turn asymmetries reflecting that of its pre-supernova circumstellar medium (Meyer et al. 2024). We hereby continue this numerical effort, by tackling the question of the mixing of the several kind of plasma participating in the constitution of the plerions.

This study is organized as follows. In Section 2, we review the simulation strategy, the different utilised methods and initial conditions used to carry out the magneto-hydrodynamical (MHD) simulations of the evolving close medium of a series of runaway high-mass stars, from the onset of their main-sequence to their supernova remnant phase. Section 3 provides a detailed description of the internal distribution of materials (stellar winds, supernova ejecta, pulsar wind) into the pulsar wind nebula produced by the moving progenitors. We particularly study the mixing at work therein. Section 4 further discusses the results, their limitation and scope. Finally, we draw our conclusions in Section 5.

## 2 METHOD

### 2.1 Simulation strategy

The global modelling of young to middle-age pulsar wind nebulae is worked in a three-steps fashion, and has a particular set of advantages and caveats.

First, the circumstellar medium generated by stellar wind-ISM interaction of the moving massive star is simulated from its zero-age main-sequence time to its pre-supernova time. The wind-ISM interaction of the progenitor is calculated in the reference frame of the moving star, and serves as the initial condition for the calculation of the interaction between the blastwave and the circumstellar medium. Secondly, the supernova blastwave, with released ejecta corresponding to the progenitor mass at the moment of the explosion, minus the mass of a canonical neutron star, is injected into freely-expanding last stellar wind and advanced in a 1-dimensional, high-resolution fashion during 50 years, which is sufficient to simulate the structure of the region of swept-up stellar gas and supernova material that progresses through the wind. Last, this 1D solution is mapped onto the 2.5-dimensional circumstellar medium, i.e. the density, velocity and pressure gas structure, described by 2 dimensions for the scalar quantities plus a toroidal component for the vectors, at the moment of the explosion, and a pulsar wind is injected at the location of the supernova. The whole evolution is then continued within the 2.5-dimensional approach.

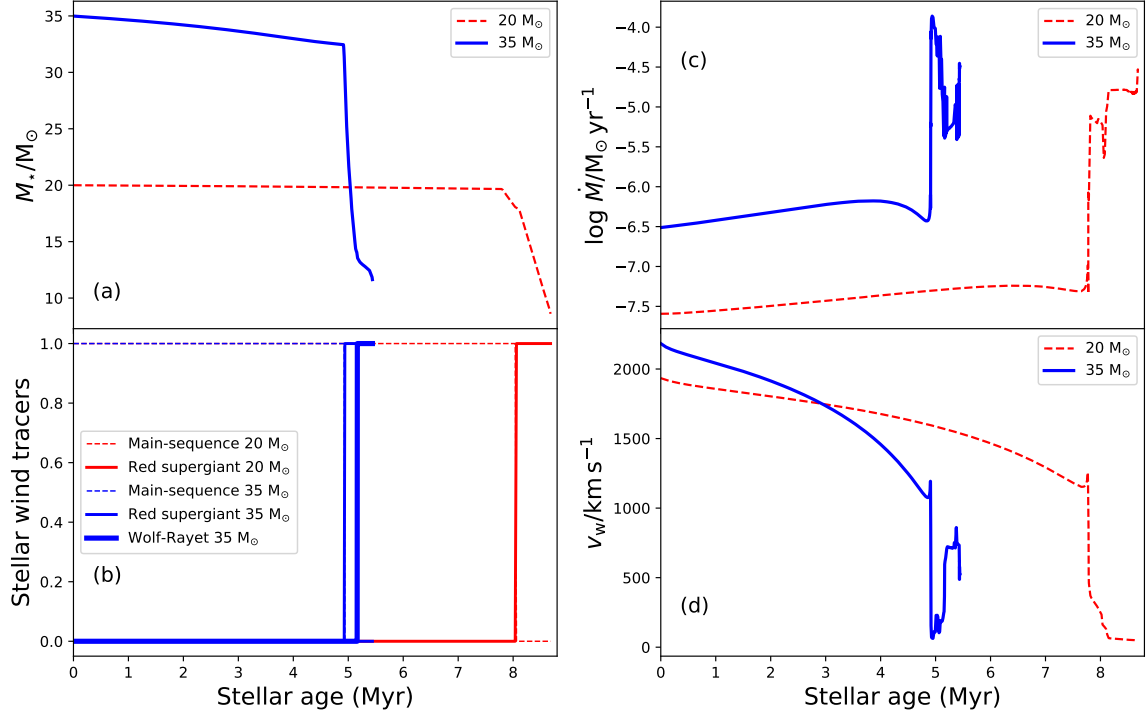


**Figure 1.** Time evolution (in Myr) of the supernova progenitors of zero-age main-sequence  $20 M_\odot$  (dotted red line) and  $35 M_\odot$  (solid blue line) which we use in our work. The figures show the mass of the stars  $M_\star$  (panel a, in  $M_\odot$ ), the values of the stellar wind tracers (panel b), their mass-loss rate  $\dot{M}$  (panel c, in  $M_\odot \text{yr}^{-1}$ ), and the wind velocity  $v_w$  (panel d, in  $\text{km s}^{-1}$ ).

The evolution of the chemical yields into supernova remnants is a profound question to investigate. The main-sequence, red supergiant and Wolf-Rayet stellar winds are tracked using a series of passive scalar tracers which values are time-dependently set to 1 throughout the corresponding stellar evolutionary phases and to 0 elsewhere. Similarly, a tracer gives access to the distribution of the supernova ejecta and another permits to follow the expanding of the pulsar wind into the supernova remnant Meyer et al. (2024,?). The passive scalar fields are evolved throughout the supernova remnants via the advection equations,

$$\frac{\partial(\rho Q_{\text{MS}})}{\partial t} + \vec{\nabla} \cdot (\vec{v} \rho Q_{\text{MS}}) = 0, \quad (1)$$

$$\frac{\partial(\rho Q_{\text{RSG}})}{\partial t} + \vec{\nabla} \cdot (\vec{v} \rho Q_{\text{RSG}}) = 0, \quad (2)$$

$$\frac{\partial(\rho Q_{\text{WR}})}{\partial t} + \vec{\nabla} \cdot (\vec{v} \rho Q_{\text{WR}}) = 0, \quad (3)$$

$$\frac{\partial(\rho Q_{\text{EJ}})}{\partial t} + \vec{\nabla} \cdot (\vec{v} \rho Q_{\text{EJ}}) = 0, \quad (4)$$

$$\frac{\partial(\rho Q_{\text{PSR}})}{\partial t} + \vec{\nabla} \cdot (\vec{v} \rho Q_{\text{PSR}}) = 0, \quad (5)$$

with  $Q_{\text{MS}}$ ,  $Q_{\text{RSG}}$ ,  $Q_{\text{WR}}$ ,  $Q_{\text{EJ}}$  and  $Q_{\text{PSR}}$  the tracers for the main-sequence, red supergiant, Wolf-Rayet stellar winds, supernova ejecta and pulsar wind material,  $\rho$  the mass density and  $v$  the gas velocity, respectively. Hence, a 2.5-dimensional plerionic supernova remnants are obtained, including a series of 5 tracers allowing us to track the

distribution of the several species involved into that problem. This approach is similar to that found in Orlando et al. (2020, 2022b). Such approach permits to reach models of high spatial resolution at moderate computational costs, which allows us to explore the parameter space of the problem.

## 2.2 Initial conditions

A spherically-symmetric stellar wind is injected onto a sphere of radius 20 cells centered into the origin of the computational domain, by imposing therein mass density and terminal velocity, evaluated from the escape wind velocity with the recipe of Eldridge et al. (2006). The stellar wind properties are interpolated from the stellar evolutionary tracks for the  $20 M_\odot$  and the  $35 M_\odot$  rotating stars of the GENEVA modes (Ekström et al. 2012), from the zero-age main-sequence to the pre-supernova times. The main stellar wind properties are reported in Fig. 1. The stellar wind terminal radial velocity is calculated via the relation,

$$v_w(t) = \sqrt{\beta(T) \frac{2GM_\star(t)}{R_\star(t)}}, \quad (6)$$

with  $G$ ,  $M_\star$  and  $R_\star$  the gravitational constant, the stellar mass, and the radius of the star. The term  $\beta(T)$  comes from the recipe of Eldridge et al. (2006). The circumstellar medium used as initial conditions is calculated assuming that the runaway progenitor is a blackbody radiator, i.e. estimating the stellar radius with its photospheric luminosity and its effective temperature, respectively, which diminishes the terminal speed during the Wolf-Rayet phase of the higher-mass progenitor (Meyer et al. 2023, 2024), making our model consistent with the values measures for weak-winded Galactic Wolf-Rayet stars, see the work of Hamann et al. (2019). The

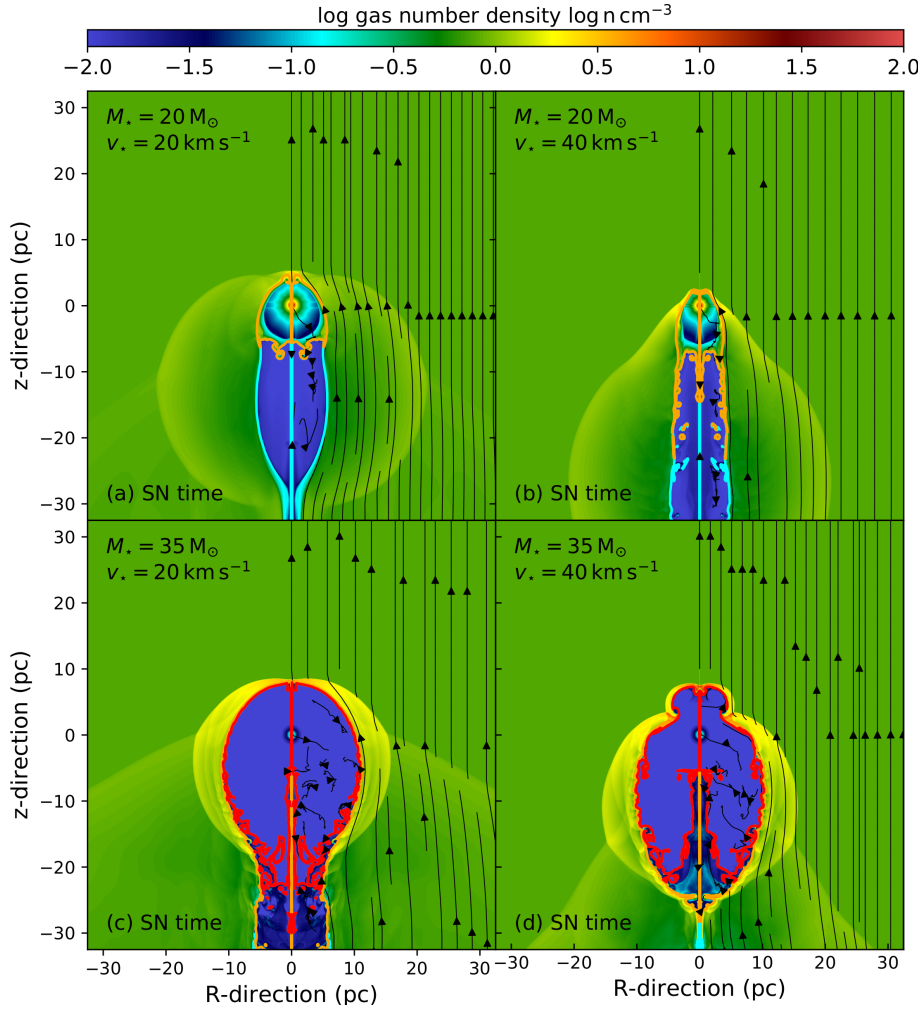


**Figure 2.** Number density fields in our magneto-hydrodynamical simulation of the circumstellar medium of the runaway stars at the supernova time. The figure displays the models for the  $20 M_{\odot}$  (top) and the  $35 M_{\odot}$  (bottom) stars moving at velocities  $v_{\star} = 20 \text{ km s}^{-1}$  (left) and  $v_{\star} = 40 \text{ km s}^{-1}$  (right). The various contours highlight the region with a 50% contribution of the Wolf-Rayet wind (red), red supergiant wind (orange) and with a 10% contribution of main-sequence material (cyan), respectively. The black arrows in the right-hand parts of the figures are ISM magnetic field lines.

initial equatorial rotational velocity of the progenitors is chosen to 10% of the star's break-up rotation rate. The magnetic field of the stars is estimated from observations for OB stars (Fossati et al. 2015; Przybilla et al. 2016) and red supergiants (Vlemmings et al. 2002; Kervella et al. 2018), superimposed into the stellar wind (Rozyczka & Franco 1996; García-Segura et al. 2018) and its strength is scaled to that of the decrease of the solar wind magnetisation as (Scherer et al. 2020; Baalman et al. 2020).

The  $10^{51}$  erg supernova explosion is modelled using the prescription of Chevalier (1982); Truelove & McKee (1999), which is set on a power-law density profile (an inner dense plateau and a decreasing envelope). Together with an homologous expansion profile for the velocity, and ejecta masses of  $7.28 M_{\odot}$  and  $10.12 M_{\odot}$  for the  $20 M_{\odot}$  and  $35 M_{\odot}$  progenitors, we implemented the onset of the blastwave as described in Whalen et al. (2008); van Veelen et al. (2009).

The profiles for the blastwave reads

$$\rho(r) = \begin{cases} \rho_{\text{core}}(r) & \text{if } r \leq r_{\text{core}}, \\ \rho_{\text{max}}(r) & \text{if } r_{\text{core}} < r < r_{\text{max}}, \end{cases} \quad (7)$$

where,

$$\rho_{\text{core}}(r) = \frac{1}{4\pi n} \frac{(10E_{\text{ej}}^{n-5})^{-3/2}}{(3M_{\text{ej}}^{n-3})^{-5/2}} \frac{1}{t_{\text{max}}^3}, \quad (8)$$

and,

$$\rho_{\text{max}}(r) = \frac{1}{4\pi n} \frac{(10E_{\text{ej}}^{n-5})^{(n-3)/2}}{(3M_{\text{ej}}^{n-3})^{(n-5)/2}} \frac{1}{t_{\text{max}}^3} \left(\frac{r}{t_{\text{max}}}\right)^{-n}, \quad (9)$$

and with the ejecta mass  $M_{\text{ej}}$ , the ejecta energy  $E_{\text{ej}}$  and  $n = 11$  (Truelove & McKee 1999; Bandiera et al. 2021). Additionally,

$$t_{\text{max}} = \frac{r_{\text{max}}}{v_{\text{max}}}, \quad (10)$$

is calculated following Whalen et al. (2008). The velocity is set as  $v(r) = r/t$  with

$$v_{\text{core}} = \left(\frac{10(n-5)E_{\text{ej}}}{3(n-3)M_{\text{ej}}}\right)^{1/2}, \quad (11)$$

and

$$v_{\text{max}} = \frac{r_{\text{max}}}{t_{\text{max}}} = 3 \times 10^4 \text{ km s}^{-1}, \quad (12)$$



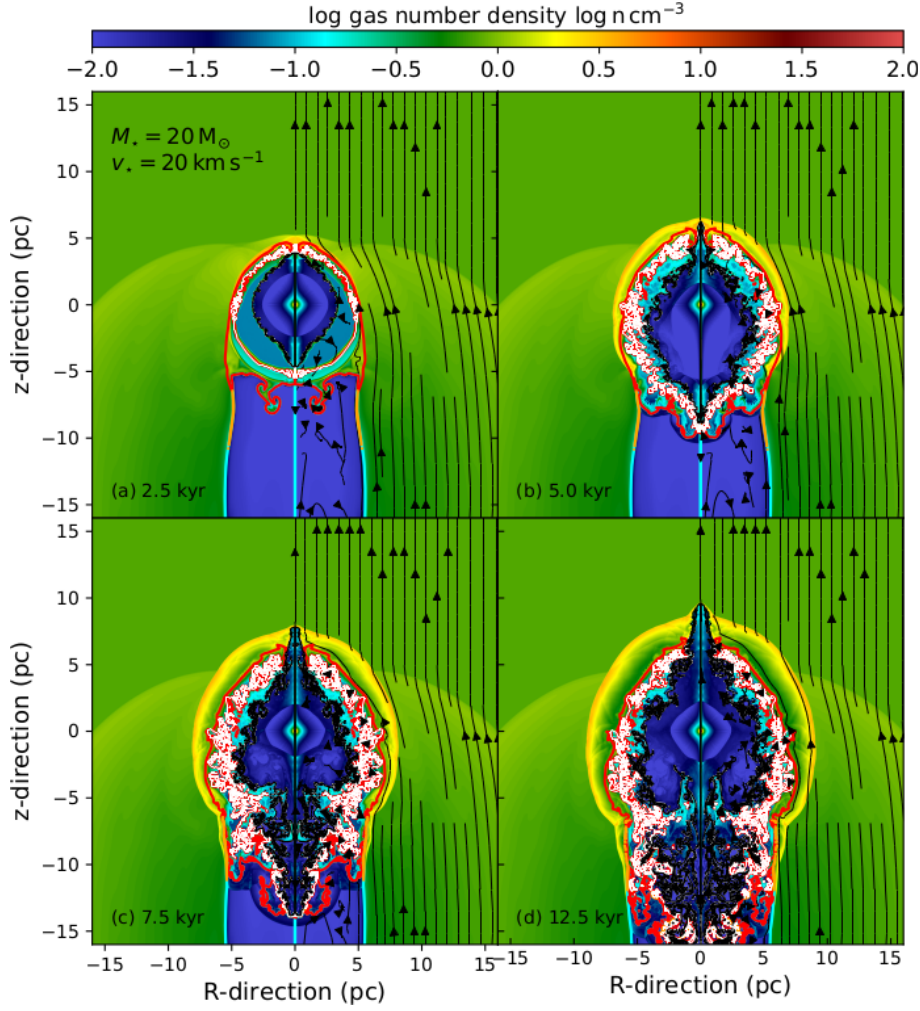


**Figure 3.** Number density fields in our magneto-hydrodynamical simulation of the supernova remnant of the runaway  $20 M_{\odot}$  star rotating with  $\Omega_{\star}/\Omega_K = 0.1$  and moving with velocity  $v_{\star} = 20 \text{ km s}^{-1}$ . The evolution of the plerionic supernova remnant is shown at times 2.5 (a), 5.0 (b), 7.5 (c) and 12.5 kyr (d), respectively. The various contours highlight the region with a 50% contribution of pulsar wind nebula (black), supernova ejecta (white), Wolf-Rayet wind (red), red supergiant wind (orange) and with a 10% contribution of main-sequence material (cyan), respectively. The black arrows in the right-hand parts of the figures are ISM magnetic field lines.

with  $t_{\text{max}} = 5.11 \times 10^{-8} \text{ Myr}$  and  $r = r_{\text{max}} = 0.00153 \text{ pc}$ . The radii marking the end of the blastwave plateau is  $r = r_{\text{core}} = 0.000212 \text{ pc}$  for  $v_{\text{core}} = 4155.2 \text{ km s}^{-1}$  in the case of the  $20 M_{\odot}$  and  $r = r_{\text{core}} = 0.000180 \text{ pc}$  for  $v_{\text{core}} = 3524.4 \text{ km s}^{-1}$  in the case of the  $35 M_{\odot}$ , respectively.

The pulsar wind is set on the prescription of Komissarov & Lyubarsky (2004). We assume the pulsar to be of initial power,

$$\dot{E}(t) = \dot{E}_0 \left(1 + \frac{t}{\tau_0}\right)^{\alpha}, \quad (13)$$

with,

$$\alpha = \frac{n+1}{n-1}, \quad (14)$$

where  $n$  is the braking index of the pulsar and where the initial spin-down is given by,

$$\tau_0 = \frac{P_0}{(n-1)\dot{P}_0}, \quad (15)$$

where following Slane (2017). We set  $\dot{E}_0 = 10^{38} \text{ erg s}^{-1}$ , with a time-dependence governed with  $n = 3$ , a period  $P_0 = 0.3 \text{ s}$  and a

period derivative  $\dot{P}_0 = 10^{-17} \text{ s s}^{-1}$ . The relativistic pulsar wind is of velocity  $0.01 c$  (Slane 2017) and its corresponding mass density is estimated with the laws presented in van der Swaluw (2003). The magnetic field associated to the pulsar wind is injected onto a sphere of radius 20 cells as,

$$B_{\text{psr}}(r, t) = \sqrt{4\pi \frac{\dot{E}(t)}{v_{\text{psr}}} \frac{\sqrt{\sigma}}{r}} \sin(\theta) \left(1 - \frac{2\theta}{\pi}\right), \quad (16)$$

where  $\sigma = 10^{-3}$  (Slane 2017) and  $v_{\text{psr}} = 0.01c$  the pulsar wind speed where  $c$  is the speed of light.

The calculations are performed in the frame of the moving progenitor, assuming two distinct bulk velocities  $v_{\star} = 20 \text{ km s}^{-1}$  and  $v_{\star} = 40 \text{ km s}^{-1}$ . We summarise the models in this study, together with their corresponding evolutionary sequence, in Table 1.

### 2.3 Numerical methods

We carry out our simulations within the frame of the magneto-hydrodynamics with the PLUTO code, presented in Mignone et al.

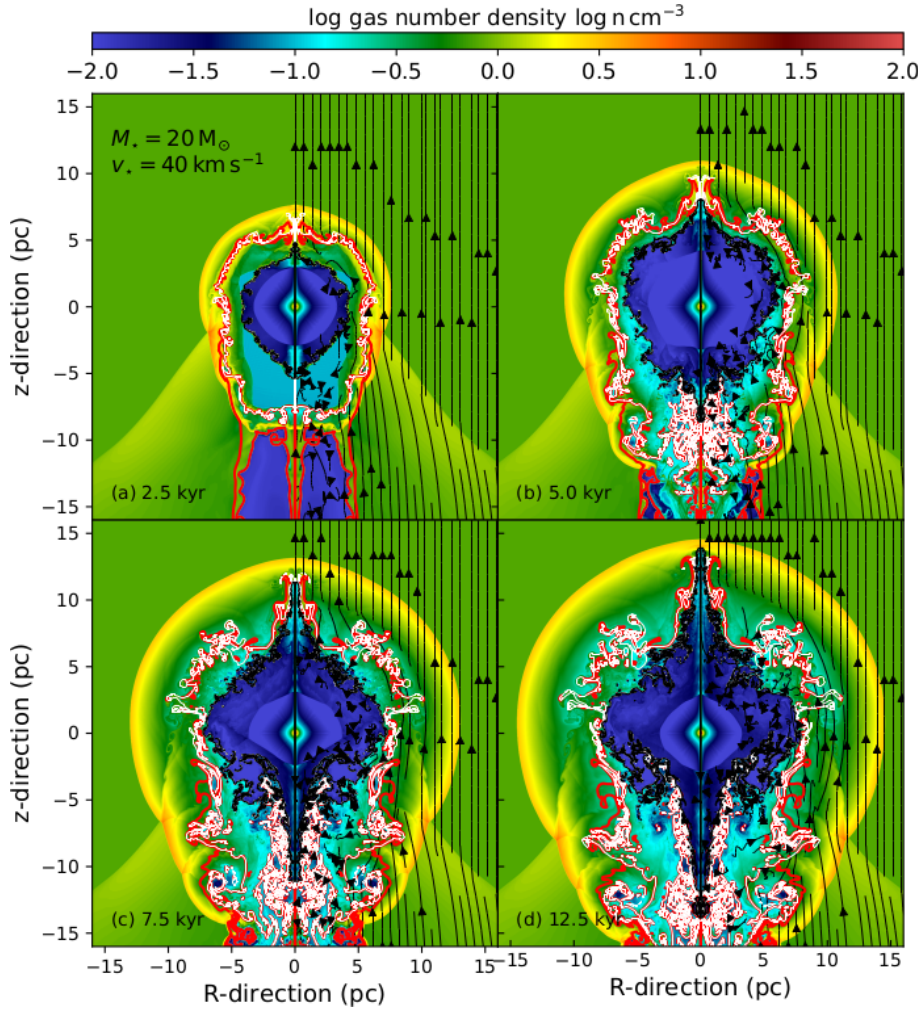


**Figure 4.** As Fig. 3 for a  $20 M_{\odot}$  progenitor star moving with velocity  $v_{\star} = 40 \text{ km s}^{-1}$ .

(2007, 2012), by solving the following set of equations:

$$\frac{\partial \rho}{\partial t} + \vec{\nabla} \cdot (\rho \vec{v}) = 0, \quad (17)$$

$$\frac{\partial \vec{m}}{\partial t} + \vec{\nabla} \cdot (\vec{m} \otimes \vec{v} - \vec{B} \otimes \vec{B} + \hat{I} p_t) = \vec{0}, \quad (18)$$

$$\frac{\partial E}{\partial t} + \vec{\nabla} \cdot ((E + p_t) \vec{v} - \vec{B}(\vec{v} \cdot \vec{B})) = \Phi(T, \rho), \quad (19)$$

$$\frac{\partial \vec{B}}{\partial t} + \vec{\nabla} \cdot (\vec{v} \otimes \vec{B} - \vec{B} \otimes \vec{v}) = \vec{0}, \quad (20)$$

with  $\rho$  is the mass density,  $\vec{v}$  the velocity vector,  $\vec{m} = \rho \vec{v}$  the momentum vector,  $\hat{I}$  the identity vector,  $\vec{B}$  the magnetic field vector,  $p_t = p + \vec{B}^2/8\pi$  the total pressure, and,

$$E = \frac{p}{(\gamma - 1)} + \frac{\vec{m} \cdot \vec{m}}{2\rho} + \frac{\vec{B} \cdot \vec{B}}{2}, \quad (21)$$

the total energy, where  $\gamma = 5/3$  the adiabatic index. The system is evolved under the assumption of an ideal equation of state and the governing equations are closed with,

$$c_s = \sqrt{\frac{\gamma p}{\rho}}, \quad (22)$$

where  $c_s$  is the sound speed of the plasma. The term

$$\Phi(T, \rho) = n_H \Gamma(T) - n_H^2 \Lambda(T), \quad (23)$$

represents the optically-thin radiative processes such as cooling and heating, where,

$$T = \mu \frac{m_H p}{k_B \rho}, \quad (24)$$

is the gas temperature, see Meyer et al. (2014). This terms are not included starting from the launching of the pulsar wind. After that moment, the system is evolved adiabatically.

The bow shock constituting the circumstellar medium of the runaway core-collapse progenitor is modelled using a 2.5-dimensional cylindrical coordinate system  $(R, z)$ . The size of the utilised computational domain is  $[0; 100] \times [-50; 50] \text{ pc}^2$  and it is mapped with a  $2000 \times 2000$  grid zones, i.e. with a uniform spatial resolution of  $\Delta = 5.0 \times 10^{-2} \text{ pc}$ . The results for the circumstellar medium are displayed in Fig. 2. The initial interaction between the supernova blastwave and the freely-expanding last stellar wind of the progenitor is calculated with a 1-dimensional spherical computational domain, mapped with a  $[0; 2.5] \text{ pc}^2$  that is uniformly discretised with 125000 grid zones, which is equivalent to a spatial resolution of  $\Delta = 2.0 \times 10^{-5} \text{ pc}$ . The simulations for the supernova remnants are performed with a 2.5-dimensional cylindrical coordinate system  $(R, z)$  (i.e., a 2 dimensional cylindrical grid for the scalar

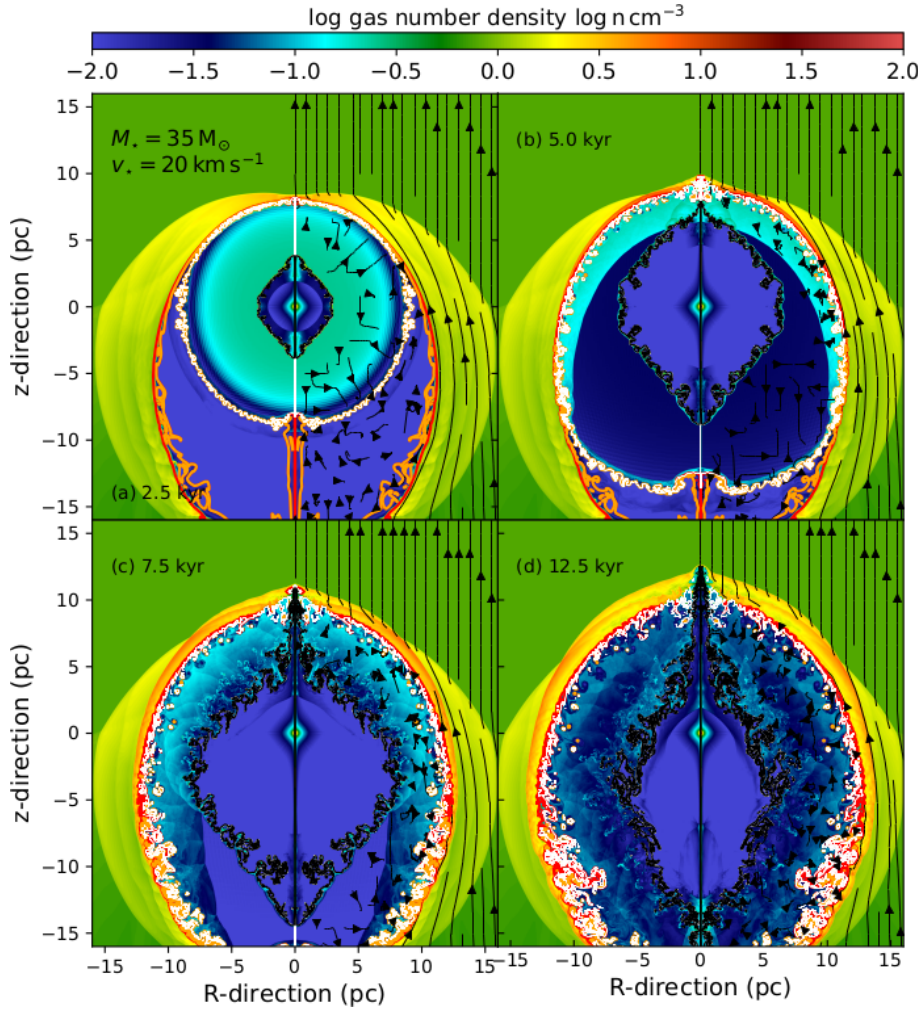


Figure 5. As Fig. 3 for a  $35 M_{\odot}$  progenitor star moving with velocity  $v_{\star} = 20 \text{ km s}^{-1}$ .

quantities plus a toroidal component for the vectors) onto which a  $[0; 25] \times [-25; 25] \text{ pc}^2$  computational domain is mapped with a  $4000 \times 8000$  grid zones, permitting to reach everywhere spatial resolution of  $\Delta = 6.25 \times 10^{-3} \text{ pc}$ .

We make use of a finite-volume, dimensionally unsplit Godunov-type solver that is made of the HLL Riemann solver (Harten et al. 1983) together with the third-order Runge-Kutta integrator for the time-marching algorithm. The spatial reconstruction of the variables between the grid zones are performed with the piecewise parabolic method of interpolation for the models for the circumstellar medium, and are performed with a linear spatial reconstruction and the minmod slope limiter for the calculations for the supernova remnants, making the later scheme total variation diminishing. The timesteps are controlled by the Courant-Friedrich-Lewy number which we initially set to 0.3. The scheme continuously ensures the divergence-free character of the magnetic field vector everywhere in the computational domain (Powell 1997). We refer interested readers on further details about the numerical method to the previous studies Meyer et al. (2024, ?).

## 3 RESULTS

### 3.1 Distribution of material in the pulsar wind nebulae

Fig. 3 plots the number density fields in our magneto-hydrodynamical simulation of the supernova remnant of a runaway  $20 M_{\odot}$  star, initially rotating with  $\Omega_{\star}/\Omega_{\text{K}} = 0.1$  and moving with velocity  $v_{\star} = 20 \text{ km s}^{-1}$ . Its evolution is shown at times 2.5 (a), 5.0 (b), 7.5 (c) and 12.5 kyr (d), respectively. The contours mark the region with a 50% contribution of supernova ejecta (white), red supergiant wind (red) and with a 10% contribution of main-sequence material (cyan), respectively. The black arrows in the right-hand parts of the figures are ISM magnetic field lines. Fig. 4 is similar as Fig. 3 for a progenitor velocity of  $v_{\star} = 40 \text{ km s}^{-1}$  and Figs. 5, 6 are for a  $35 M_{\odot}$  star with the Wolf-Rayet wind highlighted in orange.

The supernova remnant in the model with  $20 M_{\odot}$  star and  $v_{\star} = 20 \text{ km s}^{-1}$  (Fig. 3a) has the overall shape of a Napoleon’s hat, when the blastwave remains partly trapped into the red supergiant bow shock, which distributes as an arc/shell of material interacting with the main-sequence material (red). The low-density cavity behind the star is filled with main-sequence wind (cyan). The supernova material expands spherically first, then interacts asymmetrically with the circumstellar medium (white), as described in Meyer et al. (2015). The pulsar wind nebula grows inside of the ejecta as reported in van der Swaluw (2003); Komissarov & Lyubarsky (2004). When the



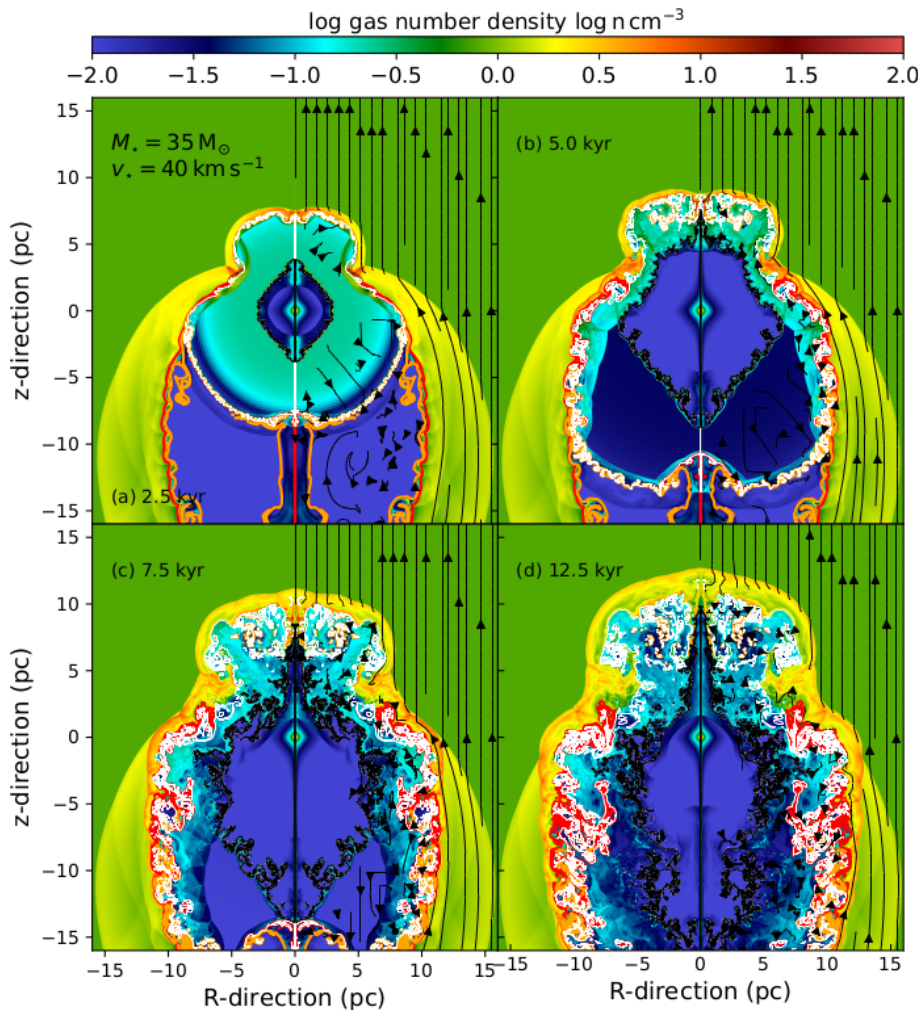


**Figure 6.** As Fig. 3 for a  $35 M_{\odot}$  progenitor star moving with velocity  $v_{\star} = 40 \text{ km s}^{-1}$ .

remnant growth, the supernova ejecta are filling a ring which outer border is the shocked dense circumstellar medium, and the inner border is the termination shock of the pulsar wind nebula which entered reverberation. Because of the density and velocity differences between the species, Rayleigh-Taylor instabilities develop in the ejecta ring (Fig. 3b). As the shock wave is channeled into the trail of the bow shock, the pulsar wind nebula adopts an oblong shape in which the leptonic wind develops strong instabilities with the other materials downstream the location of the explosion. The supernova remnant in the model with  $20 M_{\odot}$  star and  $v_{\star} = 40 \text{ km s}^{-1}$  (Fig. 4) is the model that corresponds to a Cygnus-Loop-like supernova remnant (Meyer et al. 2024) and which evolution is presented in Meyer & Meliani (2022). The ring of expanding ejecta has the drop-like morphology outflowing from the bow shock, quickly affected by strong instabilities at the ejecta/supergiant discontinuity and inducing important deviation of the pulsar wind nebulae from the solution of Komissaroff & Lyubarsky (2004).

Since the cavity carved by the Wolf-Rayet wind of the  $35 M_{\odot}$  star is larger than that of the red supergiant wind alone by the  $20 M_{\odot}$  star, then the ring of supernova ejecta expands freely in the stellar wind. This happens until reaching distances of 5 pc when it begins to interact with the shell of mixed Wolf-Rayet and red supergiant stellar wind. The pulsar wind develops as a diamond shape inside the ejecta (Fig. 5a). At the time of the reflection of the supernova

blastwave with the circumstellar medium (5.0 kyr), the pulsar wind is still unperturbed in its expansion by the external medium (Fig. 5b) and then it begins the reverberation phase, that is induced by the reflected blastwave in the northern region of the supernova remnant (Fig. 5c), accelerating the mixing of pulsar wind material and supernova ejecta in the remnant, while that of the supernova ejecta with the stellar wind diminishes. The eddies of the instabilities at the blastwave-wind interface are much smaller than that in the model with  $20 M_{\odot}$ . When the  $35 M_{\odot}$  progenitor moves with velocity  $v_{\star} = 40 \text{ km s}^{-1}$ , the circumstellar medium is smaller and more much complex, which profoundly modifies the reflection of the blastwave (Fig. 6a). The breaking of the diamond shape of the pulsar wind nebula due to the reflection of the blastwave is more pronounced, both along and opposite of the direction of motion of the progenitor (Fig. 6b,c). The reflection is more efficient and travels back closer to the center of the explosion than when  $v_{\star} = 20 \text{ km s}^{-1}$ , creating a thin region of mixed stellar winds and supernova ejecta surrounding the irregular pulsar wind nebula.

### 3.2 Mixing of materials

Fig. 7 displays the evolution of the mixing efficiency of the post-main-sequence stellar winds, i.e. red supergiant (a) and Wolf-Rayet (b), the supernova ejecta (c) and the pulsar wind (d). The quantities



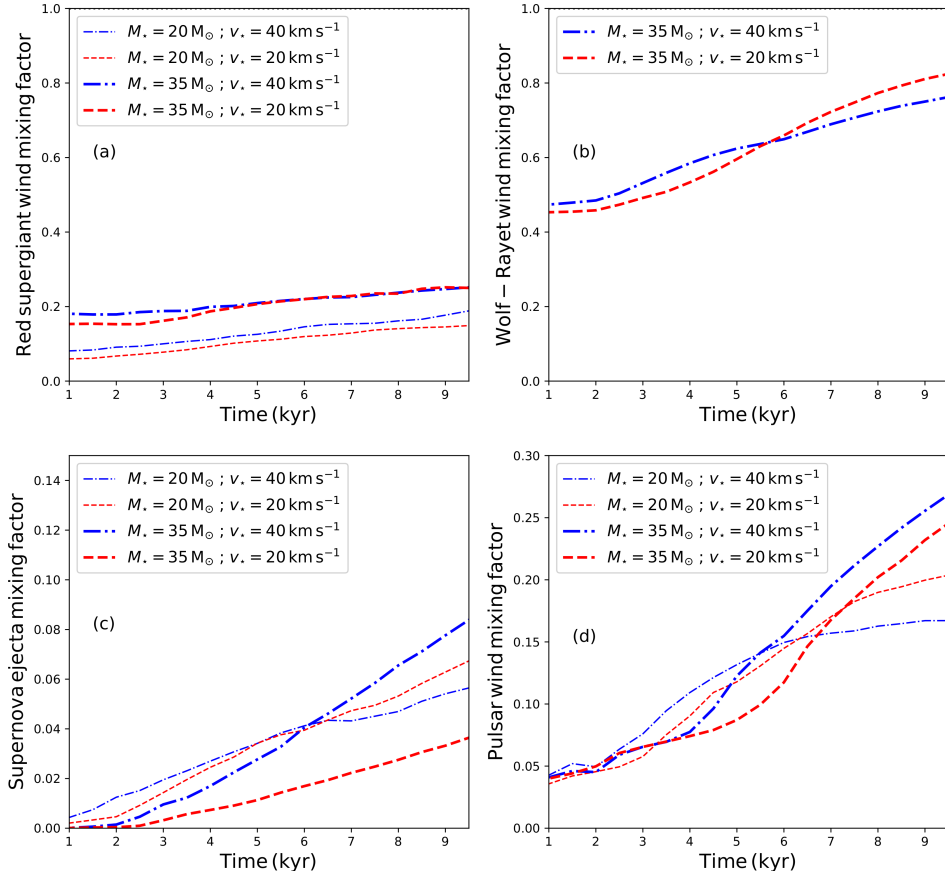


**Figure 7.** Mixing of the different materials in the plerionic supernova remnant during the first 9 kyr after the supernova explosion. The line colors distinguish models with stellar velocity  $v_{\star} = 20 \text{ km s}^{-1}$  (dashed red) and  $v_{\star} = 40 \text{ km s}^{-1}$  (dotted dashed blue), and for  $M_{\star} = 20 M_{\odot}$  (thin lines) and  $M_{\star} = 35 M_{\odot}$  (thick lines). The panels display the mixing for the red supergiant (a), Wolf-Rayet (b) wind material, supernova ejecta (c) and pulsar wind (d), respectively.

are plotted for the  $20 M_{\odot}$  (thin lines) and the  $35 M_{\odot}$  progenitor stars (thick lines), moving with velocities  $v_{\star} = 20 \text{ km s}^{-1}$  (dashed lines) and  $v_{\star} = 40 \text{ km s}^{-1}$  (dashed dotted lines). The definition of the mixing efficiency  $f_i$  of a given specie that we adopt follows the prescription of Orlando et al. (2005). They read,

$$f_{\text{MS}} = \frac{\mu_{\text{MH}} \iint_{Q_{\text{MS}} \leq 0.5} n Q_{\text{MS}} dV}{\mu_{\text{MH}} \iint_{\text{SNR}} n Q_{\text{MS}} dV} = \frac{\iint_{Q_{\text{MS}} \leq 0.5} n Q_{\text{MS}} dV}{\iint_{\text{SNR}} n Q_{\text{MS}} dV}, \quad (25)$$

$$f_{\text{RSG}} = \frac{\iint_{Q_{\text{RSG}} \leq 0.5} n Q_{\text{RSG}} dV}{\iint_{\text{SNR}} n Q_{\text{RSG}} dV}, \quad (26)$$

$$f_{\text{WR}} = \frac{\iint_{Q_{\text{WR}} \leq 0.5} n Q_{\text{WR}} dV}{\iint_{\text{SNR}} n Q_{\text{WR}} dV}, \quad (27)$$

$$f_{\text{EJ}} = \frac{\iint_{Q_{\text{EJ}} \leq 0.5} n Q_{\text{EJ}} dV}{\iint_{\text{SNR}} n Q_{\text{EJ}} dV}, \quad (28)$$

$$f_{\text{PSR}} = \frac{\iint_{Q_{\text{PSR}} \leq 0.5} n Q_{\text{PSR}} dV}{\iint_{\text{SNR}} n Q_{\text{PSR}} dV}, \quad (29)$$

respectively, where  $dV$  is the volume element of the 2.5-dimensional supernova remnant model. The integrals are performed onto the supernova remnants volume that is selected from the rest of the computational domain using a criterion based on the number density of

the unperturbed ambient medium. The denominator of each mixing factors represents the total mass of a given specie inside of the supernova remnant, and the numerator stands for the mass of a given specie in the cells that are filled with less than 50% in number density of that particular kind of material. Hence  $f_i = 0$  means that there is no mixing happening in the supernova remnant, i.e. that it is, in the average, pure with respect to that particular material  $i \in \{\text{MS}, \text{RSG}, \text{WR}, \text{EJ}, \text{PSR}\}$ , in the sense that most of its mass is made of that particular specie. When  $f_i = 1$ , that material is diluted and it contributes by  $\leq 50$  per cent in number density to the local chemical composition of the gas, see also Meyer et al. (2023).

The total amount of red supergiant wind mixes by  $\leq 20\%$ , mostly due to the fact that large quantities of this material constitute the dense circumstellar medium and has filled the low-density trail of the runaway progenitor's bow shock, which are not yet impacted by the expansion of the supernova blastwave, regardless of the progenitor's mass and/or bulk velocity. The distribution of Wolf-Rayet material is also strongly affected by the morphology of the circumstellar medium, which is rather circular if the  $35 M_{\odot}$  progenitor star moves with velocity  $20 \text{ km s}^{-1}$  as a result of the Wolf-Rayet shell forming prior to the explosion (Brighenti & D'Ercole 1995) while this region is more oblong if the star move faster. The Wolf-Rayet wind mixes efficiently by 50% to 80% within the 10 kyr after the explosion.

In this study, we will not estimate the mixing of main-sequence material into the supernova remnant, since this specie is not present anymore into the stellar wind bow shock of the progenitor for the

age that we consider ( $\approx 10$  kyr after the supernova). The mixing efficiency relative to the red supergiant material evolves from 10% to 15% in the time windows that we consider, showing a 50% difference with that in the model with  $20 M_{\odot}$  and  $35 M_{\odot}$  (Fig. 7a).

The effects of the progenitor bulk motion is much milder and even totally vanishes in the  $35 M_{\odot}$  model at times  $> 5$  kyr. The mixing efficiency of Wolf-Rayet material is only calculated for half of our simulations, since such specie is evidently not present in the evolution of the initial  $20 M_{\odot}$  star (Fig. 7b). The Wolf-Rayet material is the first specie to be immediately shocked by the blastwave, hence, its mixing efficiency increases quicker and already reaches 50% at time 1 kyr after the supernova, to have values of early 80% at time 10 kyr, respectively. The Wolf-Rayet material mixes better in the model with velocity  $40 \text{ km s}^{-1}$  until the remnant ages 5.5 kyr, then the mixing in that with velocity  $20 \text{ km s}^{-1}$  becomes more important then.

The mixing efficiency of the supernova ejecta increase from 0% to up to 8% over the time that we consider in the calculations. This quantity increases quasi-linearly in the case of a  $20 M_{\odot}$  progenitor until 6 kyr after the explosion, for both models with velocity  $20 \text{ km s}^{-1}$  and  $40 \text{ km s}^{-1}$ , the later being more important than the sooner (Fig. 7c). The mixing in the models with a  $35 M_{\odot}$  progenitor is milder until 6 kyr, however, the faster model mixes better than the slowest model. Then, the simulation with velocity  $40 \text{ km s}^{-1}$  rises quickly, reaching efficiency of 8%, as a direct consequence of the morphology of the circumstellar medium. The pulsar wind mixing efficiency evolves from 4% to 15–20% in the model with the progenitor  $20 M_{\odot}$ , while it reaches values as high as 25% in the case of the  $35 M_{\odot}$  star (Fig. 7d). At early times the mixing is more important in the red supergiant plerion, because the reverberation happens sooner since the pre-supernova bow shock is smaller. The pulsar wind recovers the X-shape in the model with  $20 M_{\odot}$  and  $40 \text{ km s}^{-1}$ , which establishes an equilibrium between the region of pulsar wind and the region of ejecta, preventing further mixing. Inversely, mixing of pulsar wind material is very inefficient in the case of the  $35 M_{\odot}$  progenitor that produced a very wide wind cavity prior to the explosion. The pulsar wind expands into the unperturbed ejecta until about 4 kyr after the explosion. Once the shock wave hits the circumstellar medium and reflects, the pulsar wind is affected accordingly especially in the northern region of the supernova remnant, which increases greatly the mixing efficiency.

All in all, our work shows that the the mixing of material in the subsequent remnant is more important in the case of higher-mass runaway star moving at high velocities.

The spatial distribution of the several tracers are further displayed at a selected time of the evolution of the pulsar wind nebulae in Fig. 8 (models with velocity  $20 \text{ km s}^{-1}$ ) and in Fig. 9 (models with velocity  $40 \text{ km s}^{-1}$ ), respectively. Horizontal (top panels) and vertical (bottom panels) cuts are taken through the supernova remnants generated by the supernova progenitor moving with  $v_{\star} = 20 \text{ km s}^{-1}$  prior to the explosion. The slices are along the R-direction direction (top figure) and along the z-direction (bottom figure). In each figure, the panel (a) concerns the  $20 M_{\odot}$  progenitor star and the panel (b) concerns the  $35 M_{\odot}$  progenitor star, respectively. The panels represent the number density (dashed purple line, in  $\text{cm}^{-3}$ ), the main-sequence (cyan), red supergiant (orange), Wolf-Rayet (red), supernova ejecta (green) and pulsar wind (black) material tracers. The figures further illustrates that the most important mixing region is the location of the supernova remnants that are perpendicular to the direction of motion of the progenitor, where the blastwave meets the former stellar wind bow shock. It is clearly seen that the mixing of material is stronger in the case of a heavy progenitor star (see Fig. 8a,b and Fig. 9a,b),

moving at high bulk velocity through the ISM prior to the explosion (see Fig. 8a and Fig. 9a, Fig. 8b and Fig. 9b).

## 4 DISCUSSION

### 4.1 Limitations of the models

#### 4.1.1 Axisymmetry, wind speed and magnetisation

The 2.5-dimensional framework (with two spatial dimensions for the computational grid and three for the vectorial quantities) implies that any inclination of the supernova progenitor's rotational axis with respect to its direction of motion is not treatable. Similarly, the pulsar's spin axis in relation to the massive star's movement and the local ISM magnetic field orientation are also not considered. Thus all the directions of the ISM magnetic field, progenitor's bulk motion, progenitor axis of rotation and pulsar axis of rotation are dictated by the symmetry axis of the cylindrical coordinate system (Chita et al. 2008; van Marle et al. 2012; Chiotellis et al. 2021). Although this approach improves computational efficiency and yields useful insights into plerionic supernova remnants, it falls short of capturing the full complexity of these phenomena. Producing full 3-dimensional models (Herbst et al. 2020; Velázquez et al. 2023) would enable the inclusion of factors such as independent directions of motion and rotation of both the progenitor, respectively, as well as the pulsar bulk motion and update the works of Kolb et al. (2017); Temim et al. (2017, 2022).

The most prominent effect generated by the use of the above-described 2.5-dimensional coordinate system is the development of artificial jet-like features along the symmetry axis. These features appear when a source of momentum with a component parallel to the axis encounters a counterflow in its own reference frame. This situation arises in various cases, such as the bow shock of a massive runaway star (Comerón & Kaper 1998), the wind bubble of a static OB star (Dwarkadas 2007), a protostellar jet (Mattia et al. 2023), a supernova blast wave (Franco et al. 1991; Balsara et al. 2008), or a pulsar wind nebula (Komissarov & Lyubarsky 2004). This effect is further intensified by the presence of magnetic fields in the simulation (Meyer et al. 2017), by cooling mechanisms (Meyer et al. 2017), or by the radiative transport of ionizing emissions from the stellar object (Comerón 1997). In our present setup, combining a supersonic stellar wind, a runaway stellar object, a blast wave driven by a core-collapse supernova explosion, and the subsequent launch of a pulsar wind provides all the ingredients for the simulation models to develop such jet-like artifacts, as seen in Figs. 3, 4, 5, 6, and 12. As these features grow over time, they become more visible at times  $\geq 10$  kyr. Discriminating between the artificial nature of these jet-like features and the development of physical structures, such as the polar jet of a pulsar wind nebula, would require full 3D simulations with high spatial resolution (Meyer et al. 2021), which is beyond the scope of this paper.

The pulsar wind nebulae that we examine in our study are treated within the non-relativistic framework. By performing classical numerical magnetohydrodynamical simulations, we make use of a considerably slower pulsar wind speed that values corresponding to the high Lorentz factors that can be reached by such objects, see Kennel & Coroniti (1984). A more stable simulation environment is achieved, which is better suited for long-term numerical investigations of supernova remnant and pulsar wind nebula problem. We are aware that a lower pulsar wind speed and/or its low magnetisation induce several drawbacks, particularly regarding the compression rates and shock speeds with the remnant and also the emergence of associated

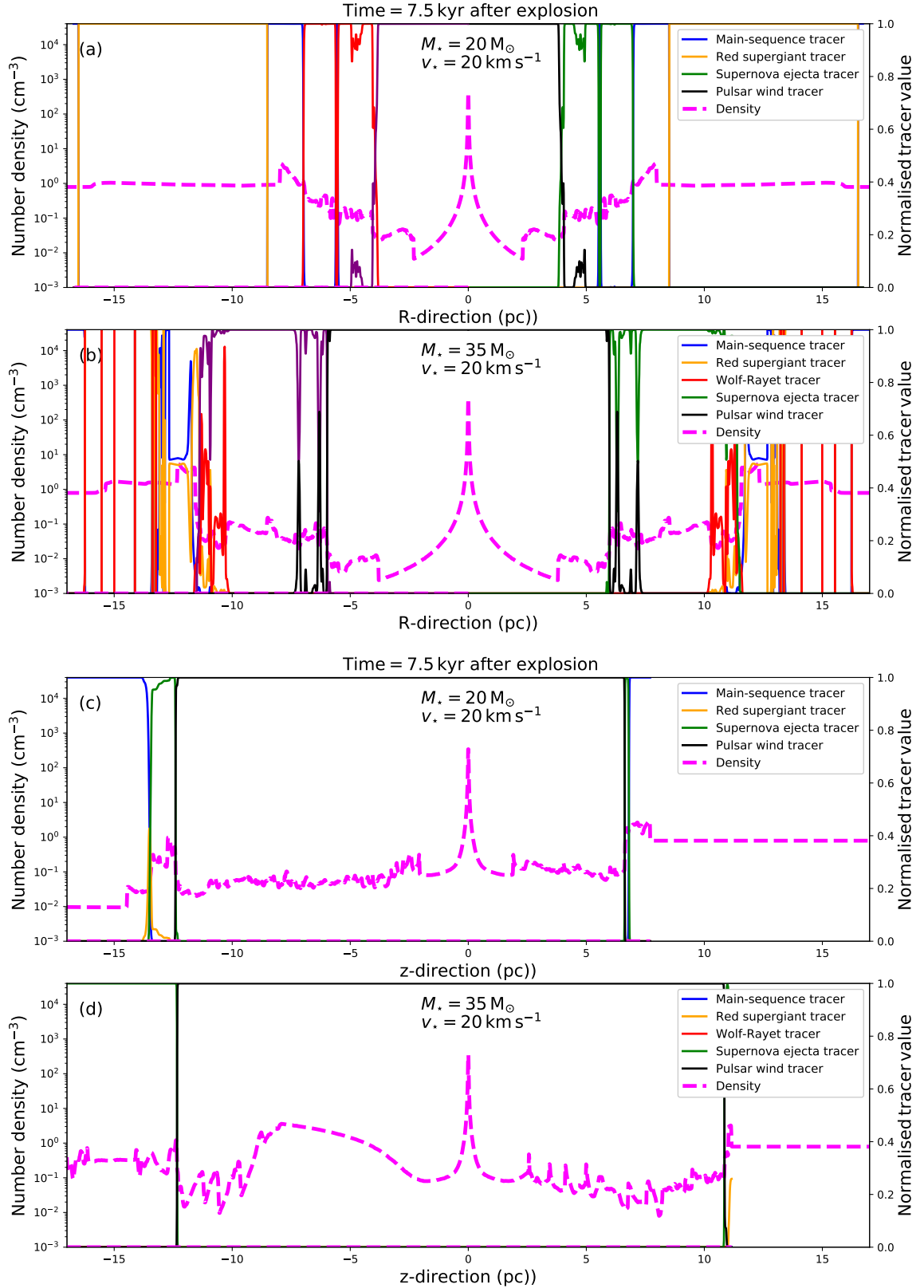


**Figure 8.** Cuts taken through the supernova remnants generated by the supernova progenitor moving with  $v_* = 20 \text{ km s}^{-1}$  prior to the explosion. The slices are along the R-direction direction (top figure) and along the z-direction (bottom figure). In each figure, the panel (a) concerns the  $20 M_\odot$  progenitor star and the panel (b) concerns the  $35 M_\odot$  progenitor star, respectively. The panels represent the number density (dashed purple line, in  $\text{cm}^{-3}$ ), the main-sequence (cyan), red supergiant (orange), Wolf-Rayet (red), supernova ejecta (green) and pulsar wind (black) material tracers.

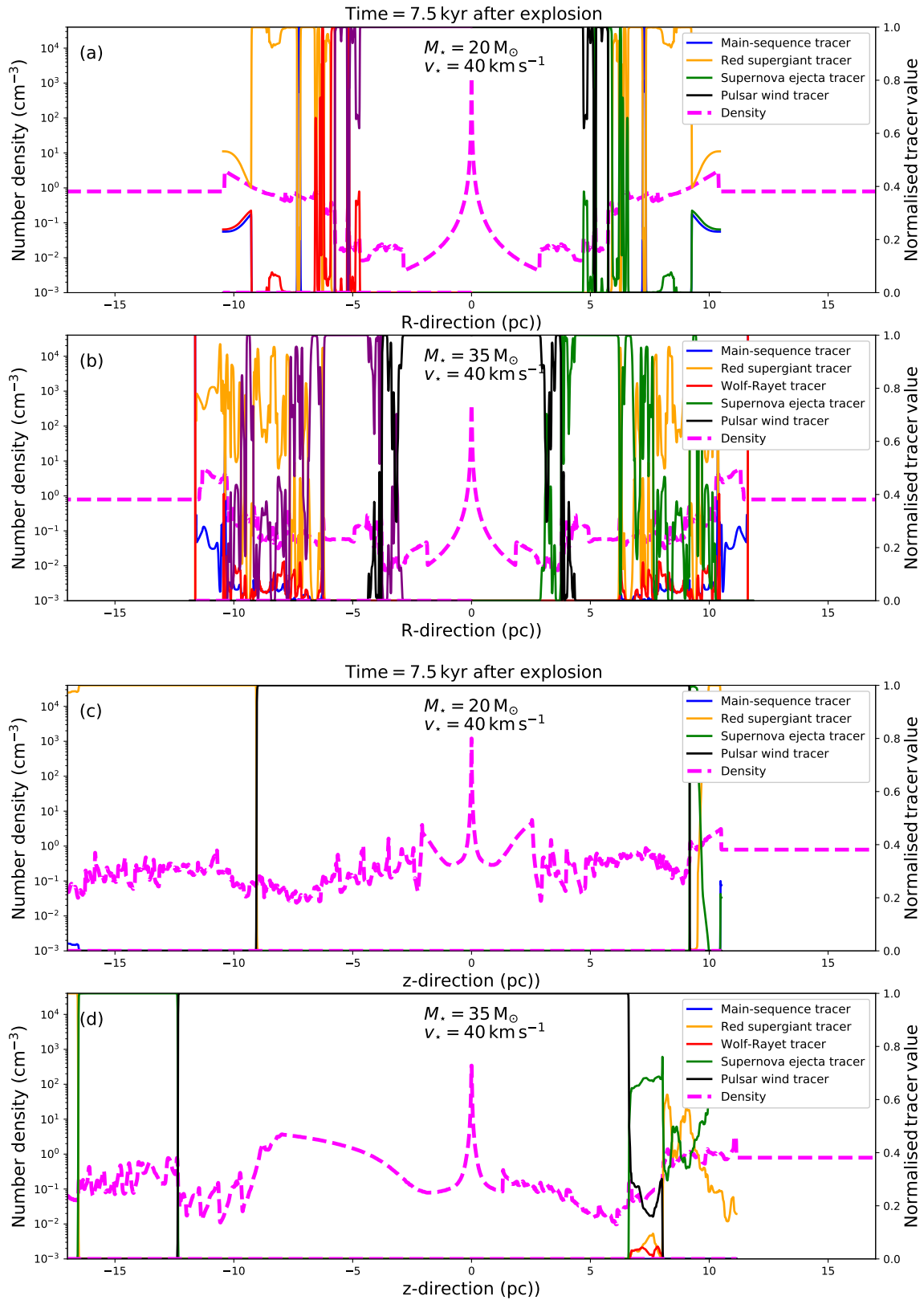


**Figure 9.** As Fig. 8 for progenitor stars moving with velocity  $v_* = 40 \text{ km s}^{-1}$  prior to the explosion.



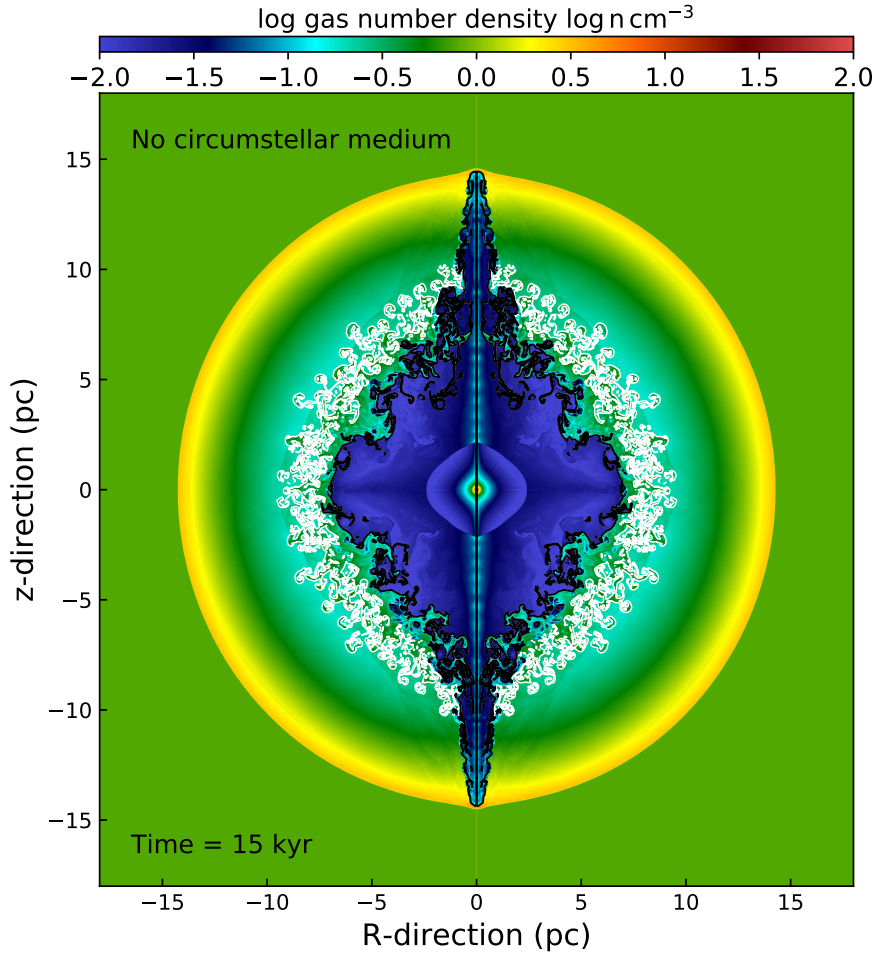


**Figure 10.** Number density field in a magneto-hydrodynamical simulation of the supernova remnant of a  $20 M_{\odot}$  star rotating with  $\Omega_{\star}/\Omega_K = 0.1$  and moving with velocity  $v_{\star} = 20 \text{ km s}^{-1}$ . The evolution of the plerionic supernova remnant is shown at 15 kyr after the explosion. The various contours highlight the region with a 50% contribution of pulsar wind (black) and supernova ejecta (white).

instabilities at the contact discontinuities in them. Our solution then applies to rather very weak-winded pulsars, however, they offer a first insight into the physics of material mixing in pulsar wind nebulae. Moreover, via the additional hypothesis that a substantial fraction of the magnetic field energy is transformed into kinetic energy in the pulsar wind nebulae, we assume in this study a low magnetization parameter of  $\sigma = 10^{-3}$ , following the precedent works of [Kennel & Coroniti \(1984\)](#); [Slane \(2017\)](#); [Begelman & Li \(1992\)](#). We are aware that other numerical works showed that higher possible values of  $\sigma \gg 0.01$  can be better suited for the explanation of the observational feature of some pulsar wind nebulae, see for example [Porth et al. \(2014\)](#). This corner of the parameter space is still to be explored, the present study being more focused on the presentation of a method to study mixing in plerions, rather than on a systematic investigation of that question and/or on the tailoring of models to a specific object. This will be investigated in a forthcoming study.

#### 4.1.2 Other limitations

Another class of improvement to be brought in our simulations concerns the initial conditions and the included microphysical processes.

The pristine environment in which the progenitor high-mass stars move are still extremely simplified in the present models. Amongst others, the multi-phased nature of the ISM ([McKee & Ostriker 1977](#)) is to affect the development of pre-supernova wind nebulae such as the bow shocks that our runaway stars induce ([Baalmann et al. 2021](#)). In turn, this will affect the subsequent blastwave-nebula interaction ([Miceli et al. 2013](#)) and eventually the old, large-scale remnant and its emission properties ([Das et al. 2024](#)). Including this element would provide a more accurate representation of the interaction between the pulsar wind and its surrounding environment. Moreover, considering the oblique rotating pulsar magnetosphere would enhance the accuracy of the simulated characteristics of pulsar wind nebulae, such as particle acceleration ([Pétri 2022](#)) and non-thermal emission mechanisms see [Philippov & Spitkovsky \(2018\)](#). These improvements are essential for advancing our understanding and present propitious directions for future research.

Last, the current model investigate mixing of materials by use of passive scalars that are advected throughout the expanding supernova remnants and pulsar wind nebulae [Meyer et al. \(2023\)](#), i.e. the time-dependent chemical evolution of the yields blown in the stellar winds and released in the ejecta are not included. This will request the

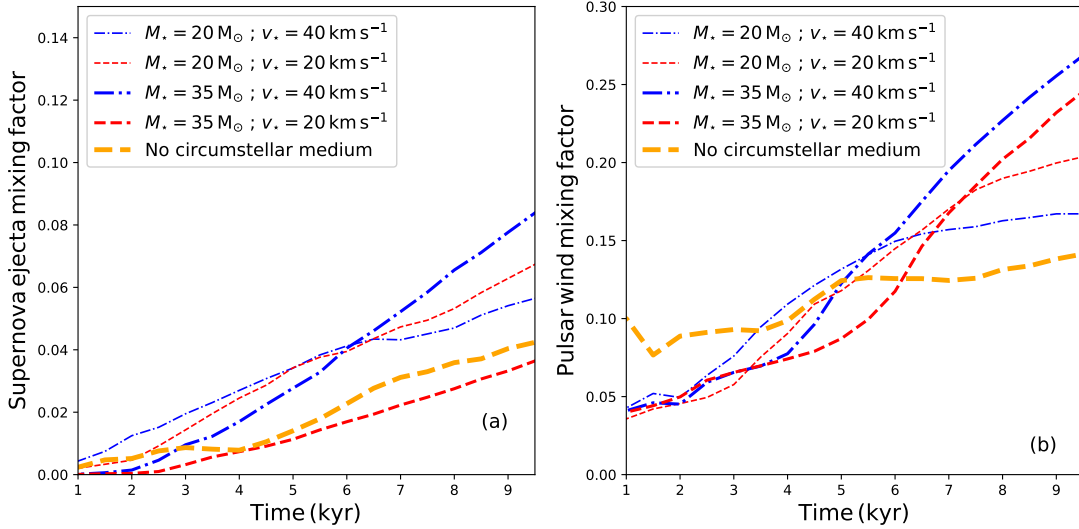


**Figure 11.** Mixing of the different materials in the plerionic supernova remnant considered without circumstellar medium (orange line). The line colors distinguish between the other models with stellar velocity  $v_{\star} = 20 \text{ km s}^{-1}$  (dashed red) and  $v_{\star} = 40 \text{ km s}^{-1}$  (dotted dashed blue), and for  $M_{\star} = 20 M_{\odot}$  (thin lines) and  $M_{\star} = 35 M_{\odot}$  (thick lines). The panels display the mixing for the supernova ejecta (a) and pulsar wind (b), respectively.

coupling of the magneto-hydrodynamical models to a full chemical network Grassi et al. (2014); Katz (2022) that change each species number density as a result of their natural interaction within the conditions of pressure and temperature in the remnant (Zhou et al. 2022). Such models are highly desirable and we hope to present them in the future.

#### 4.2 The role of the circumstellar medium

Fig. 10 displays the number density field in a magneto-hydrodynamical simulation of the supernova remnant of the  $20 M_{\odot}$  progenitor star moving with velocity  $v_{\star} = 20 \text{ km s}^{-1}$ , but excluding the influence of the wind-ISM interaction, i.e. the circumstellar nebula is not included into the calculation. The evolution of the plerionic supernova remnant is shown at times 15 kyr after the explosion and the two contours highlight the region with a 50% contribution of pulsar wind (black) and supernova ejecta (white). The expansion of the forward shock of the blastwave is not constrained by the circumstellar medium and the overall supernova remnant adopts a circular morphology. Inside of it, the contact discontinuity between the pulsar wind and the supernova ejecta is affected by the Richtmyer-Meshkov instability, a particular case of the Rayleigh-Taylor instability (Kane et al. 1999). The pulsar wind nebula produces the typical morphology that is described by the work of Komissarov & Lyubarsky (2004), with a diamond-like shape made of an equatorial ring and a vertical jet which propagation throughout the ejecta is magnified along the symmetry axis of the simulation domain. Note that a model of this kind has been presented in the work of Meyer & Meliani (2022) where it is shown that the presence of the circumstellar medium greatly affects the synchrotron radio emission signature of the pulsar wind nebulae.

In Fig. 11 the mixing efficiency of the supernova ejecta and of the pulsar wind material of the plerion calculated excluding the circumstellar medium is plotted (thick dashed orange line) together with the other calculations including a runaway progenitor. The mixing

efficiency of the pulsar wind nebula without wind-ISM interaction is lower than that of the other models, except for the simulation with a  $35 M_{\odot}$  progenitor star moving with velocity  $v_{\star} = 20 \text{ km s}^{-1}$  (red dashed line of Fig. 11a). This is due to the very large cavity which is produced by the Wolf-Rayet stellar wind (Fig. 5), permitting the blastwave to expand into a low-density medium during more time than in the other models before beginning to interact with the circumstellar medium. The mixing of the ejecta is therein slightly lower than when the blastwave is exploding into the warm phase of the ISM, which is denser than the Wolf-Rayet cavity in Fig. 5. The evolution of the mixing efficiency of the pulsar wind material is initially larger than in the other simulations, however, when the supernova blastwave hits the stellar wind bow shock of the defunct progenitor and is reflected towards the center of the explosion, this translates into a stronger mixing than when the circumstellar medium is ignored (Fig. 11b). The presence of a complex medium at the moment of the explosion is therefore a factor that enhances mixing of material in plerionic supernova remnants.

#### 4.3 The role of the pulsar wind

Fig. 12 displays the evolution of the mixing efficiency of the post-main-sequence stellar winds, i.e. red supergiant (a,b) and Wolf-Rayet (c,d), the supernova ejecta (e,f), considered without (left panels) and with (right panels). The quantities are plotted for the  $20 M_{\odot}$  (thin lines) and the  $35 M_{\odot}$  progenitor stars (thick lines), moving with velocities  $v_{\star} = 20 \text{ km s}^{-1}$  (dashed lines) and  $v_{\star} = 40 \text{ km s}^{-1}$  (dashed dotted lines).

To this end, additional numerical simulations without pulsar wind nebula are performed, using the same computational domains, initial conditions, boundary conditions and microphysical processes than in the models presented above. The absence of a pulsar wind following the supernova explosion mainly turns into the fact that the supernova blastwave, once interacting with the circumstellar medium of the progenitor, can freely reflect towards the center of the explosion,

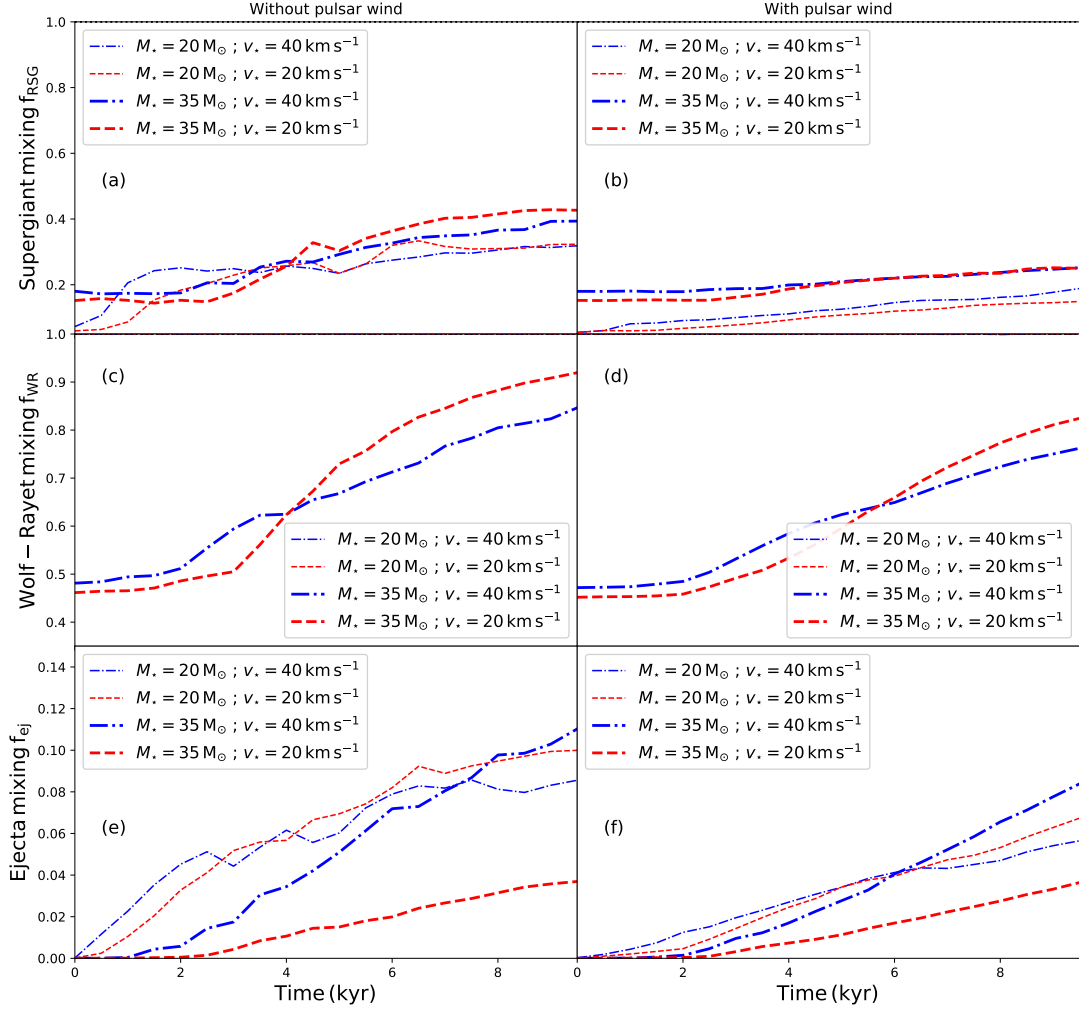


**Figure 12.** Mixing of the evolved stellar wind (top, middle panels) and supernova ejecta (bottom panels) materials in the plerionic supernova remnants, considered without (left) and with (right) pulsar wind. The line colors distinguish between the other models with stellar velocity  $v_* = 20 \text{ km s}^{-1}$  (dashed red) and  $v_* = 40 \text{ km s}^{-1}$  (dotted dashed blue), and for  $M_* = 20 M_\odot$  (thin lines) and  $M_* = 35 M_\odot$  (thick lines).

filling the interior of the supernova remnant (Meyer et al. 2015; Chiotellis et al. 2021; Meyer et al. 2023). As a consequence, the mixing efficiency is higher without pulsar wind (Fig. 12a) than with it (Fig. 12b), which reduces it by a factor of 2 approximately. The same is true for the Wolf-Rayet stellar wind that reaches values to a mixing efficiency of 0.9 to 0.8 after 9 kyr, see Fig. 12c,d. Last, the mixing efficiency of the supernova ejecta are also affected by the absence of a pulsar wind, see the differences between its values in Fig. 12e,f, which are lower in the plerionic case than in the case of supernova remnants without pulsar wind in them. We can conclude from this analysis that the presence of a pulsar wind nebula in a supernova remnant has a global effect consisting in diminishing the mixing of materials in it.

The detailed consequence of the pulsar wind blowing into the supernova remnant does not change the respective importance of the mixing efficiency of the red supergiant wind once the remnant is 7 kyr old, in the sense that this material in the models with a  $35 M_\odot$  Wolf-Rayet progenitor star mix better than in the models with a red supergiant star (Fig. 12a,b). The same is true for the Wolf-Rayet stellar wind, which is more important in the model with velocity  $v_* = 20 \text{ km s}^{-1}$  than in the simulation with velocity  $v_* = 40 \text{ km s}^{-1}$ ,

see Fig. 12c,d, and for the supernova ejecta, see Fig. 12e,f. Most notable difference between the simulations with and without pulsar wind in them happen in the early evolution phase of the system, before that the blastwave hits the pre-supernova wind bubble and that the pulsar wind termination shock reverberates, at times  $\leq 4$ –5 kyr after the explosion. Fluctuations in the time evolution of the mixing efficiency are particularly present in the models with a  $20 M_\odot$  progenitor, as it produces a smaller bow shock prior to the explosion, provoking quick reflection of the blastwave and reverberation of the pulsar wind.

#### 4.4 Mixing and emission properties of supernova remnants: towards possible future improvements

We have shown that the stellar wind history of massive stars, in addition to shaping their circumstellar medium prior to the explosion and governing the expansion of the supernova blastwave, also dictates the morphology of supernova remnants. This wind history is also responsible for the distribution of chemical elements within the remnants. The hydrogen-burning products from the main-sequence and red supergiant winds, the C, N, and O elements blown into the Wolf-Rayet

material, and the heavy elements such as Mg, Si, Ca, Ti, and Fe in the supernova ejecta (Gabler et al. 2021), mix together through a series of shock-producing wave reflections and transmissions. The final distribution of chemical yields is therefore the outcome of a complex process that begins at the onset of the main-sequence phase, coupling stellar evolution with the local conditions of the interstellar medium. Once the star has exploded, this process is powered by the pulsar wind from the magnetized neutron star formed during the core-collapse explosion and hosted by the remnant. Understanding the precise locations of these chemical elements and their relative number densities enables us to determine the types of emissions they produce and the intensity of their fluxes. For example, main-sequence material emits  $H\alpha$  at 6564 Å, evolved stellar winds produce atomic spectral lines such as the optical [N II] at 6584 Å and the [S II] doublet at 6716 and 6731 Å. The forbidden [O III] line at 5007 Å (Mavromatakis 2003) and the O, Mg, and Fe elements generate soft X-ray emission in the keV energy band (Orlando et al. 2019).

The approach we present here is primitive in that the tracers associated with each one of the species are passively advected with the plasma. In reality, chemical elements interact and undergo a variety of physical-chemical reactions, influenced by local temperature conditions. These reactions alter their abundances, resulting in the destruction of some atoms and the creation of new molecules, such as dust particles. The level of detail in the chemical reaction model directly impacts how closely the solution matches actual observations. Several numerical methods have been developed to address this complexity. The PLUTO code, for instance, includes a limited network of chemical elements and reactions, allowing for non-equilibrium calculations of the ionization balance of various species. This approach is used to derive the appropriate gas cooling through collisionally excited line radiation (Mignone et al. 2007; Teşileanu et al. 2008; Mignone et al. 2012). Similar methods, which also consider photo-heating of gas by stellar ionizing radiation, have been presented by Toalá & Arthur (2011). The KROME package allows users to define custom species and reactions, enabling the study of specific chemical phenomena when coupled with magneto-hydrodynamics (Grassi et al. 2014). The distribution of chemical yields can be further analyzed using radiative transfer post-processing tools, which convert them into local emissivity maps, projected maps, and spectra.

Lastly, we take a closer look at the method derived by in the study of historical supernova remnants, such as Cas A () and SN1987a (), which utilizes the same magneto-hydrodynamical code as ours. High spatial resolution is achieved through a remapping routine that enables calculation of the supernova blastwave's expansion into the stellar wind and circumstellar medium, while maintaining a constant number of grid zones. This approach provides an equivalent of the expanding grid used in codes such as ZEUS (van Marle et al. 2010) for the PLUTO code. This mapping scheme includes tracers for ions such as H, He, C, O, Ne, Mg, Si, Ca, Ti, Ni, and Fe, provided by a self-consistent explosion simulation that incorporates neutrino physics, as shown by Gabler et al. (2021). By further accounting for line centroid shifts and broadening due to the Doppler effect, thermal broadening of emission lines, and uniform photoelectric absorption from the interstellar medium, one can, with the integration of a Boltzmann equation, obtain temperature and abundance profiles. These profiles allow synthesis of spectra using a non-equilibrium emission model, resulting in realistic X-ray spectra in the keV energy band (Orlando et al. 2019, 2020, 2022b, 2024). This procedure bridges the gap between simulations incorporating chemical reactions and synthetic observations, paving the way for a feedback loop of numerical experiments that converge on tailored models for specific astrophys-

ical objects. Our research direction, focused on studying plerionic supernova remnants, will continue along these lines in the future.

## 5 CONCLUSION

This research examines the influence of the circumstellar medium produced by a rotating, magnetized high-mass star that is exiled through the ISM exerts onto the mixing of the different kind of materials involved in the pulsar wind nebula developing inside of the supernova remnant formed after the explosive death of those runaway massive stars. The study presented aimed at determining the evolution of the spatial distribution of the progenitor's stellar winds, supernova ejecta, pulsar leptonic wind, and to quantify the manner they mix and melt into the remnant. The simulations were performed in the 2.5-dimensional magneto-hydrodynamical fashion, using the PLUTO code (Mignone et al. 2007, 2012), with the microphysical processes and implementation described in Meyer et al. (2023). The progenitors of the supernova remnants are considered to have formed into the warm phase of the Galactic plane of the Milky Way, to have been ejected and to move supersonically therein prior to finish their lives as a supernova.

The considered progenitors are chosen to be the most common core-collapse supernova progenitors. The selection takes into account their zero-age main-sequence mass ( $20 M_{\odot}$  and  $35 M_{\odot}$ ) according to the initial mass function (Kroupa 2001), and bulk velocities ( $20 \text{ km s}^{-1}$  and  $40 \text{ km s}^{-1}$ ) that bracket the peak of the velocity distribution of runaway OB stars (Blaauw 1993; Renzo et al. 2019), see also discussion regarding the initial conditions in Meyer et al. (2024). The pulsar we consider presents energetics and timing features corresponding to that of Slane (2017) and is to be taken as an example of the parameter space.

The simulation reveal the following main results.

- The total amount of red supergiant wind mixes by  $\leq 20\%$ , mostly due to the fact that large quantities of this material constitute the dense circumstellar medium and has filled the low-density trail of the runaway progenitor's bow shock, which are not yet impacted by the expansion of the supernova blastwave, regardless of the progenitor's mass and/or bulk velocity. This material is rich in H burning products which govern the  $H\alpha$  emission continuum of the supernova remnants.

- The distribution of Wolf-Rayet material is also strongly affected by the morphology of the circumstellar medium, which is rather circular if the  $35 M_{\odot}$  progenitor star moves with velocity  $20 \text{ km s}^{-1}$  as a result of the Wolf-Rayet shell forming prior to the explosion (Brighenti & D'Ercole 1995) while this region is more oblong if the star move faster. The Wolf-Rayet wind mixes efficiently by 50% to 80% within the 10 kyr after the explosion. The Wolf-Rayet material is enhanced in C, N, O elements, responsible for optical forbidden lines such as [N II] and [O III].

- The distribution of the supernova ejecta conserve sphericity for longer time if the progenitor moved with velocity  $20 \text{ km s}^{-1}$ , while it expands as complex patterns if the star moved faster, as a consequence of its earlier interaction with the circumstellar stellar wind bow shock. The ejecta mixing is more important for fast Wolf-Rayet progenitors (8%) than for slower stars (4%), whereas it is sensibly the same (6%) in the context of a red supergiant progenitor. The supernova ejecta, composed elements such as Mg, Si, Ca, Ti and Fe, induce soft keV emission and infrared photons, which can be observable.

- Similarly, the pulsar wind mixes efficiently if the progenitor was Wolf-Rayet a star (25%) than if it was a red supergiant star (20%).



• The presence of a pulsar wind inside of a supernova remnant diminishes the mixing efficiency of the stellar wind and supernova ejecta in it.

Our study shows that the past stellar and circumstellar evolution of massive stars govern the internal chemistry of their plerionic supernova remnants, which is a preponderant element to include in interpreting observations and deciphering the formation of these objects.

## ACKNOWLEDGEMENTS

The author thankfully acknowledges RES resources provided by BSC in MareNostrum to AECT-2024-2-0002. The authors gratefully acknowledge the computing time made available to them on the high-performance computer "Lise" at the NHR Center NHR@ZIB. The latter center is jointly supported by the Federal Ministry of Education and Research and the state governments participating in the NHR ([www.nhr-verein.de/unsere-partner](http://www.nhr-verein.de/unsere-partner)). This work has been supported by the grant PID2021-124581OB-I00 funded by MCIU/AEI/10.13039/501100011033 and 2021SGR00426 of the Generalitat de Catalunya. This work was also supported by the Spanish program Unidad de Excelencia María de Maeztu CEX2020-001058-M and by the European Union NextGeneration program (PRTR-C17.I1).

## DATA AVAILABILITY

This research made use of the PLUTO code developed at the University of Torino by A. Mignone (<http://plutocode.ph.unito.it/>). The figures have been produced using the Matplotlib plotting library for the Python programming language (<https://matplotlib.org/>). The data underlying this article will be shared on reasonable request to the corresponding author.

## REFERENCES

Avedisova V. S., 1972, *Soviet Ast.*, 15, 708  
 Baalmann L. R., Scherer K., Fichtner H., Kleimann J., Bomans D. J., Weis K., 2020, *A&A*, 634, A67  
 Baalmann L. R., Scherer K., Kleimann J., Fichtner H., Bomans D. J., Weis K., 2021, *A&A*, 650, A36  
 Balsara D. S., Bendinelli A. J., Tilley D. A., Massari A. R., Howk J. C., 2008, *MNRAS*, 386, 642  
 Bandiera R., Bucciantini N., Martín J., Olmi B., Torres D. F., 2020, *MNRAS*, 499, 2051  
 Bandiera R., Bucciantini N., Martín J., Olmi B., Torres D. F., 2021, *MNRAS*, 508, 3194  
 Bandiera R., Bucciantini N., Martín J., Olmi B., Torres D. F., 2023, *MNRAS*  
 Bandiera R., Bucciantini N., Olmi B., Torres D. F., 2023, *MNRAS*, 525, 2839  
 Begelman M. C., 1998, *ApJ*, 493, 291  
 Begelman M. C., Li Z.-Y., 1992, *ApJ*, 397, 187  
 Berlanas S. R., Herrero A., Comerón F., Simón-Díaz S., Cerviño M., Pasquali A., 2018, *A&A*, 620, A56  
 Blaauw A., 1993, in Cassinelli J. P., Churchwell E. B., eds, *Massive Stars: Their Lives in the Interstellar Medium* Vol. 35 of *Astronomical Society of the Pacific Conference Series*, *Massive Runaway Stars*. p. 207  
 Bock D. C. J., Turtle A. J., Green A. J., 1998, *AJ*, 116, 1886  
 Brighenti F., D'Ercole A., 1995, *MNRAS*, 273, 443  
 Brott I., Evans C. J., Hunter I., de Koter A., Langer N., Dufton P. L., Cantiello M., Trundle C., Lennon D. J., de Mink S. E., Yoon S.-C., Anders P., 2011, *A&A*, 530, A116

Bucciantini N., 2018, *MNRAS*, 478, 2074  
 Bucciantini N., Bandiera R., 2001, *A&A*, 375, 1032  
 Bühler R., Blandford R., 2014, *Reports on Progress in Physics*, 77, 066901  
 Camus N. F., Komissarov S. S., Bucciantini N., Hughes P. A., 2009, *MNRAS*, 400, 1241  
 Caswell J. L., 1979, *MNRAS*, 187, 431  
 Chevalier R. A., 1982, *ApJ*, 258, 790  
 Chiotellis A., Boumis P., Spetsieri Z. T., 2021, *MNRAS*, 502, 176  
 Chita S. M., Langer N., van Marle A. J., García-Segura G., Heger A., 2008, *A&A*, 488, L37  
 Comerón F., 1997, *A&A*, 326, 1195  
 Comerón F., Kaper L., 1998, *A&A*, 338, 273  
 Coroniti F. V., 1990, *ApJ*, 349, 538  
 Cox N. L. J., Kerschbaum F., van Marle A.-J., Decin L., Ladjal D., Mayer A., Groenewegen M. A. T., van Eck S., Royer P., Ottensamer R., Ueta T., Jorissen A., Mecina M., Meliani Z., Luntzer A., Blommaert J. A. D. L., Posch T., Vandenbussche B., Waelkens C., 2012, *A&A*, 537, A35  
 Das S., Brose R., Pohl M., Meyer D. M. A., Sushch I., 2024, *A&A*, 689, A9  
 Dearborn D. S. P., Blake J. B., 1984, *ApJ*, 277, 783  
 Del Zanna L., Volpi D., Amato E., Bucciantini N., 2006, *A&A*, 453, 621  
 Dwarakadas V. V., 2007, *ApJ*, 667, 226  
 Ekström S., Georgy C., Eggenberger P., Meynet G., Mowlavi N., Wyttenbach A., Granada A., Decressin T., Hirschi R., Frischknecht U., Charbonnel C., Maeder A., 2012, *A&A*, 537, A146  
 Eldridge J. J., Genet F., Daigne F., Mochkovitch R., 2006, *MNRAS*, 367, 186  
 Fossati L., Castro N., Morel T., Langer N., Briquet M., Carroll T. A., Hubrig S., Nieva M. F., Oskinova L. M., Przybilla N., Schneider F. R. N., Schöller M., Simón-Díaz S., Ilyin I., de Koter A., Reisenegger A., Sana H., 2015, *A&A*, 574, A20  
 Frail D. A., Scharringhausen B. R., 1997, *ApJ*, 480, 364  
 Franco J., Tenorio-Tagle G., Bodenheimer P., Rozyczka M., 1991, *PASP*, 103, 803  
 Gabler M., Wongwathanarat A., Janka H.-T., 2021, *MNRAS*, 502, 3264  
 Gaensler B. M., Slane P. O., 2006, *ARA&A*, 44, 17  
 García-Segura G., Ricker P. M., Taam R. E., 2018, *ApJ*, 860, 19  
 Gómez-González V. M. A., Rubio G., Toalá J. A., Guerrero M. A., Sabin L., Todt H., Gómez-Llanos V., Ramos-Larios G., Mayya Y. D., 2022, *MNRAS*, 509, 974  
 Grassi T., Bovino S., Schleicher D. R. G., Prieto J., Seifried D., Simoncini E., Gianturco F. A., 2014, *MNRAS*, 439, 2386  
 Gull T. R., Sofia S., 1979, *ApJ*, 230, 782  
 Gvaramadze V. V., Menten K. M., Kniazev A. Y., Langer N., Mackey J., Kraus A., Meyer D. M.-A., Kamiński T., 2014, *MNRAS*, 437, 843  
 Hamann W. R., Gräfener G., Liermann A., 2006, *A&A*, 457, 1015  
 Hamann W. R., Gräfener G., Liermann A., Hainich R., Sander A. A. C., Shenar T., Ramachandran V., Todt H., Oskinova L. M., 2019, *A&A*, 625, A57  
 Harten A., Lax P. D., van Leer B., 1983, *SIAM Review*, 25, 35  
 Herbst K., Scherer K., Ferreira S. E. S., Baalmann L. R., Engelbrecht N. E., Fichtner H., Kleimann J., Strauss R. D. T., Moeketsi D. M., Mohamed S., 2020, *ApJ*, 897, L27  
 Hester J. J., 2008, *ARA&A*, 46, 127  
 Janka H.-T., Melson T., Summa A., 2016, *Annual Review of Nuclear and Particle Science*, 66, 341  
 Kane J., Drake R. P., Remington B. A., 1999, *ApJ*, 511, 335  
 Kargaltsev O., Durant M., Pavlov G. G., Garmire G., 2012, *ApJS*, 201, 37  
 Kargaltsev O., Pavlov G., 2007, *Ap&SS*, 308, 287  
 Kargaltsev O., Pavlov G. G., Klingler N., Rangelov B., 2017a, *Journal of Plasma Physics*, 83, 635830501  
 Kargaltsev O., Pavlov G. G., Klingler N., Rangelov B., 2017b, *Journal of Plasma Physics*, 83, 635830501  
 Katz H., 2022, *MNRAS*, 512, 348  
 Kennel C. F., Coroniti F. V., 1984, *ApJ*, 283, 710  
 Kervella P., Decin L., Richards A. M. S., Harper G. M., McDonald I., O'Gorman E., Montargès M., Homan W., Ohnaka K., 2018, *A&A*, 609, A67  
 Kolb C., Blondin J., Slane P., Temim T., 2017, *ApJ*, 844, 1  
 Komissarov S. S., 2006, *MNRAS*, 367, 19

- Komissarov S. S., Lyubarsky Y. E., 2003, *MNRAS*, 344, L93
- Komissarov S. S., Lyubarsky Y. E., 2004, *MNRAS*, 349, 779
- Komissarov S. S., Lyutikov M., 2011, *MNRAS*, 414, 2017
- Kroupa P., 2001, *MNRAS*, 322, 231
- Maeder A., 2009, *Physics, Formation and Evolution of Rotating Stars*, springer-verlag edn. Astronomy and Astrophysics Library
- Maeder A., Meynet G., 2000, *ARA&A*, 38, 143
- Marcolino W., Bouret J. C., Martins F., Hillier D. J., 2024, *A&A*, 690, A318
- Martizzi D., Faucher-Giguère C.-A., Quataert E., 2015, *MNRAS*, 450, 504
- Mattia G., Del Zanna L., Bugli M., Pavan A., Ciolfi R., Bodo G., Mignone A., 2023, *A&A*, 679, A49
- Mavromatakis F., 2003, *A&A*, 398, 153
- McKee C. F., Cowie L. L., 1975, *ApJ*, 195, 715
- McKee C. F., Ostriker J. P., 1977, *ApJ*, 218, 148
- Meyer D. M.-A., Gvaramadze V. V., Langer N., Mackey J., Boumis P., Mohamed S., 2014, *MNRAS*, 439, L41
- Meyer D. M.-A., Langer N., Mackey J., Velázquez P. F., Gusdorf A., 2015, *MNRAS*, 450, 3080
- Meyer D. M.-A., Mackey J., Langer N., Gvaramadze V. V., Mignone A., Izzard R. G., Kaper L., 2014, *MNRAS*, 444, 2754
- Meyer D. M. A., Meliani Z., 2022, *MNRAS*, 515, L29
- Meyer D. M. A., Meliani Z., Velázquez P. F., Pohl M., Torres D. F., 2024, *MNRAS*, 527, 5514
- Meyer D. M. A., Mignone A., Petrov M., Scherer K., Velázquez P. F., Boumis P., 2021, *MNRAS*, 506, 5170
- Meyer D. M. A., Pohl M., Petrov M., Egberts K., 2023, *MNRAS*, 521, 5354
- Meyer D. M. A., Velázquez P. F., Pohl M., Egberts K., Petrov M., Villagran M. A., Torres D. F., Batzofin R., 2024, *A&A*, 687, A127
- Meyer D. M. A., Vorobyov E., 2024, arXiv e-prints, p. arXiv:2405.19905
- Meyer D. M. A., Vorobyov E. I., Elbakyan V. G., Stecklum B., Eisloffel J., Sobolev A. M., 2019, *MNRAS*
- Meyer D. M.-A., Vorobyov E. I., Kuiper R., Kley W., 2017, *MNRAS*, 464, L90
- Miceli M., Orlando S., Reale F., Bocchino F., Peres G., 2013, *MNRAS*, 430, 2864
- Mignone A., Bodo G., Massaglia S., Matsakos T., Tesileanu O., Zanni C., Ferrari A., 2007, *ApJS*, 170, 228
- Mignone A., Zanni C., Tzeferacos P., van Straalen B., Colella P., Bodo G., 2012, *ApJS*, 198, 7
- Mokiem M. R., de Koter A., Evans C. J., Puls J., Smartt S. J., Crowther P. A., Herrero A., Langer N., Lennon D. J., Najjarro F., Villamariz M. R., Vink J. S., 2007, *A&A*, 465, 1003
- Noriega-Crespo A., van Buren D., Cao Y., Dgani R., 1997, *AJ*, 114, 837
- Olmí B., Del Zanna L., Amato E., Bandiera R., Bucciantini N., 2014, *MNRAS*, 438, 1518
- Olmí B., Del Zanna L., Amato E., Bucciantini N., Mignone A., 2016, *Journal of Plasma Physics*, 82, 635820601
- Orlando S., Miceli M., Patnaude D. J., Plucinsky P. P., Lee S. H., Badenes C., Janka H. T., Wongwathanarat A., Raymond J., Sasaki M., Churazov E., Khabibullin I., Bocchino F., Castro D., Millard M., 2024, arXiv e-prints, p. arXiv:2408.12462
- Orlando S., Miceli M., Petruk O., Ono M., Nagataki S., Aloy M. A., Mimica P., Lee S. H., Bocchino F., Peres G., Guarrasi M., 2019, *A&A*, 622, A73
- Orlando S., Ono M., Nagataki S., Miceli M., Umeda H., Ferrand G., Bocchino F., Petruk O., Peres G., Takahashi K., Yoshida T., 2020, *A&A*, 636, A22
- Orlando S., Peres G., Reale F., Bocchino F., Rosner R., Plewa T., Siegel A., 2005, *A&A*, 444, 505
- Orlando S., Wongwathanarat A., Janka H. T., Miceli M., Nagataki S., Ono M., Bocchino F., Vink J., Milisavljevic D., Patnaude D. J., Peres G., 2022a, arXiv e-prints, p. arXiv:2202.01643
- Orlando S., Wongwathanarat A., Janka H. T., Miceli M., Nagataki S., Ono M., Bocchino F., Vink J., Milisavljevic D., Patnaude D. J., Peres G., 2022b, *A&A*, 666, A2
- Orlando S., Wongwathanarat A., Janka H. T., Miceli M., Ono M., Nagataki S., Bocchino F., Peres G., 2021, *A&A*, 645, A66
- Pétri J., 2022, *MNRAS*, 512, 2854
- Philippov A. A., Spitkovsky A., 2018, *ApJ*, 855, 94
- Popov M. V., Andrianov A. S., Burgin M. S., Zuga V. A., Rudnitskii A. G., Smirnova T. V., Soglasnov V. A., Fadeev E. N., 2019, *Astronomy Reports*, 63, 391
- Porth O., Komissarov S. S., Keppens R., 2013, *MNRAS*, 431, L48
- Porth O., Komissarov S. S., Keppens R., 2014, *MNRAS*, 438, 278
- Powell K. G., 1997, *An Approximate Riemann Solver for Magnetohydrodynamics*. Springer Berlin Heidelberg, Berlin, Heidelberg, pp 570–583
- Przybilla N., Fossati L., Hubrig S., Nieva M. F., Järvinen S. P., Castro N., Schöller M., Ilyin I., Butler K., Schneider F. R. N., Oskinova L. M., Morel T., Langer N., de Koter A., BOB Collaboration 2016, *A&A*, 587, A7
- Reach W. T., Rho J., Tappe A., Pannuti T. G., Brogan C. L., Churchwell E. B., Meade M. R., Babler B., Indebetouw R., Whitney B. A., 2006, *AJ*, 131, 1479
- Renzo M., Zapartas E., de Mink S. E., Götzberg Y., Justham S., Farmer R. J., Izzard R. G., Toonen S., Sana H., 2019, *A&A*, 624, A66
- Reynolds S. P., Chevalier R. A., 1984, *ApJ*, 278, 630
- Rozyczka M., Franco J., 1996, *ApJ*, 469, L127
- Scherer K., Baalmann L. R., Fichtner H., Kleimann J., Bomans D. J., Weis K., Ferreira S. E. S., Herbst K., 2020, *MNRAS*, 493, 4172
- Schulreich M. M., Feige J., Breitschwerdt D., 2023, *A&A*, 680, A39
- Seok J. Y., Koo B.-C., Onaka T., 2013, *ApJ*, 779, 134
- Slane P., 2017, in Alsabti A. W., Murdin P., eds., *Handbook of Supernovae*. p. 2159
- Smartt S. J., 2009, *ARA&A*, 47, 63
- Smith L. J., Pettini M., Dyson J. E., Hartquist T. W., 1984, *MNRAS*, 211, 679
- Teşileanu O., Mignone A., Massaglia S., 2008, *A&A*, 488, 429
- Temim T., Slane P., Kolb C., Blondin J., Hughes J. P., Bucciantini N., 2015, *ApJ*, 808, 100
- Temim T., Slane P., Plucinsky P. P., Gelfand J., Castro D., Kolb C., 2017, *ApJ*, 851, 128
- Temim T., Slane P., Raymond J. C., Patnaude D., Murray E., Ghavamian P., Renzo M., Jacovich T., 2022, *ApJ*, 932, 26
- Toalá J. A., Arthur S. J., 2011, *ApJ*, 737, 100
- Toropina O. D., Romanova M. M., Lovelace R. V. E., 2019, *MNRAS*, 484, 1475
- Truelove J. K., McKee C. F., 1999, *ApJS*, 120, 299
- Turner J. D., Stappers B. W., Carli E., Barr E. D., Becker W., Behrend J., Breton R. P., Buchner S., Burgay M., Champion D. J., Chen W., Clark C. J., Horn D. M., Keane E. F., Kramer M., Künkel L., Levin L., Men Y. P., Padmanabh P. V., Ridolfi A., Venkatraman Krishnan V., 2024, *MNRAS*, 531, 3579
- Uchida H., Tsunemi H., Katsuda S., Kimura M., Kosugi H., 2009, *PASJ*, 61, 301
- van der Swaluw E., 2003, *A&A*, 404, 939
- van der Swaluw E., Achterberg A., Gallant Y. A., Downes T. P., Keppens R., 2003, *A&A*, 397, 913
- van der Swaluw E., Downes T. P., Keegan R., 2004, *A&A*, 420, 937
- van Marle A. J., Meliani Z., Marcowith A., 2012, *A&A*, 541, L8
- van Marle A. J., Smith N., Owocki S. P., van Veelen B., 2010, *MNRAS*, 407, 2305
- van Veelen B., Langer N., Vink J., García-Segura G., van Marle A. J., 2009, *A&A*, 503, 495
- Velázquez P. F., Meyer D. M. A., Chiotellis A., Cruz-Álvarez A. E., Schneiter E. M., Toledo-Roy J. C., Reynoso E. M., Esquivel A., 2023, *MNRAS*, 519, 5358
- Vink J. S., Sander A. A. C., 2021, *MNRAS*, 504, 2051
- Vlemmings W. H. T., Diamond P. J., van Langevelde H. J., 2002, *A&A*, 394, 589
- Weaver R., McCray R., Castor J., Shapiro P., Moore R., 1977, *ApJ*, 218, 377
- Weiler K. W., Panagia N., 1980, *A&A*, 90, 269
- Weiler K. W., Shaver P. A., 1978, *A&A*, 70, 389
- Whalen D., van Veelen B., O’Shea B. W., Norman M. L., 2008, *ApJ*, 682, 49
- Whiteoak J. B. Z., Green A. J., 1996, *A&AS*, 118, 329
- Wiersma R. P. C., Schaye J., Smith B. D., 2009, *MNRAS*, 393, 99
- Wilkin F. P., 1996, *ApJ*, 459, L31
- Wolfire M. G., McKee C. F., Hollenbach D., Tielens A. G. G. M., 2003, *ApJ*, 587, 278
- Zhou P., Zhang G.-Y., Zhou X., Arias M., Koo B.-C., Vink J., Zhang Z.-Y.,

Sun L., Du F.-J., Zhu H., Chen Y., Bovino S., Lee Y.-H., 2022, *ApJ*, 931, 144

This paper has been typeset from a  $\text{\TeX}/\text{\LaTeX}$  file prepared by the author.